Alkaline magmas in zones of continental convergence: The Tezhsar volcano-intrusive ring complex, Armenia

Krzysztof Sokół[1,2], Ralf Halama[1*], Khachatur Meliksetian[3], Ivan P. Savov[4], Gevorg Navasardyan[3], Masafumi Sudo[5]

[1] School of Geography, Geology and the Environment, Keele University, Keele, ST5 5BG, United Kingdom

[2] (Present address) School of Earth and Environmental Sciences, University of St Andrews, St Andrews, KY16 9AL, United Kingdom

[3] Institute of Geological Sciences, Armenian National Academy of Sciences, 24a Marshal Baghramian Avenue, 0019, Yerevan, Republic of Armenia

[4] School of Earth and Environment, University of Leeds, Leeds, LS2 9JT, United Kingdom

[5] Institute of Earth and Environmental Science, University of Potsdam, Karl-Liebknecht-Str. 24-25, 14476 Potsdam, Germany

* Corresponding author contact information:

Ralf Halama

School of Geography, Geology and the Environment

Keele University

Keele, ST5 5BG, United Kingdom

E-mail: r.halama@keele.ac.uk

Phone: +44 (0) 1782 7 34960

Abstract

Alkaline igneous rocks are relatively rare in settings of tectonic convergence and little is known about their petrogenesis in these settings. This study aims to contribute to a better understanding of the formation of alkaline igneous rocks by an investigation of the Tezhsar volcano-intrusive alkaline ring complex (TAC) in the Armenian Lesser Caucasus, which is located between the converging Eurasian and Arabian plates. We present new petrological, geochemical and Sr-Nd isotope data for the TAC to constrain magma genesis and magma source characteristics. Moreover, we provide a new $^{40}Ar/^{39}Ar$ age of 41.0±0.5 Ma on amphibole from a nepheline syenite that is integrated into the regional context of ongoing regional convergence and widespread magmatism.

The TAC is spatially concentric and measures ~10 km in diameter representing the relatively shallow plumbing system of a major stratovolcano juxtaposed by ring faulting with its extrusive products. The plutonic units comprise syenites and nepheline syenites, whereas the extrusive units are dominated by trachytic-phonolitic rocks. The characteristic feature of the TAC is the development of pseudomorphs after leucite in all types of the volcanic, subvolcanic and intrusive alkaline rocks.

Whole-rock major element data show a metaluminous (Alkalinity Index = 0-0.1), alkalic and silica-undersaturated (Feldspathoid Silica-Saturation Index <0) character of the TAC. The general trace element enrichment and strong fractionation of REEs (La_N/Yb_N up to 70) indicate a relatively enriched magma source and small degrees of partial melting. All TAC rocks show a negative Nb-Ta anomalies typical of subduction zone settings. The initial $^{87}Sr/^{86}Sr$ ratios (0.704-0.705) and positive εNd values (+3 to +5) indicate an isotopically depleted upper mantle and lack of significant crustal influence, which in turn suggests the TAC magma has formed via differentiation from lithospheric mantle melts.

Regionally, the age of ~41 Ma places the TAC amid a Lesser Caucasian Eocene period of dominantly calc-alkaline magmatism. The TAC's arc-like geochemical signatures are interpreted to result from prior subduction of the Tethyan slab beneath the Eurasian continental margin. The alkaline character, distinct from regional trends, is attributed to Neotethyan slab rollback causing extension and inducing small degrees of decompression melting of metasomatised lithospheric mantle.

Keywords: Alkaline igneous rocks, ring complex, Armenia, geochemistry, $^{40}Ar/^{39}Ar$ dating, pseudoleucite

1. Introduction

Studies of alkaline magmatism on the global scale have become a point of focus due to the significant role of alkaline magmatic rocks for ore exploration, in particular regarding prospecting for rare earth elements (REEs), niobium (Nb), tantalum (Ta) and zirconium (Zr) (e.g. Chakhmouradian and Zaitsev 2012). Many alkaline igneous rocks are found in rift-related intraplate settings (e.g. Gardar Province/Greenland, Upton et al. 2003; Kola Alkaline Province/Russia, Downes et al. 2005; East African Rift, Woolley 2001), but they also occur, albeit less frequently, in settings of plate convergence (Burke and Khan, 2006; Hou et al. 2006). Plate convergence includes collisional events that cause the welding of terranes into continental land and subsequent post-collisional episodes in which convergence continues (Bonin et al. 1998). The occurrence of magmas with alkaline affinities becomes more common only when the geodynamic context becomes entirely intraplate in a post-orogenic episode (Bonin et al. 1998). In complex collisional and post-collisional settings, the timing of specific types of magmatism depends on the geotectonic geometries and the relative rates of crustal thickening and subsidiary subduction (Harris et al. 1986). Importantly, convergent movement between colliding plates will continue for 30-50 Ma after the initial collision (Harris et al. 1986). On a global scale, deformed alkaline rocks and carbonatites (DARCs) may be used as indicators of where ancient oceans have opened and closed, and the presence of a variety of syenites, carbonatites and other alkaline igneous rocks found in proximity to older DARCs indicate the recycling of material from the underlying lithosphere based on the Wilson Cycle-type model (Burke and Khan 2006). Thus, investigating alkaline magmatism in convergent settings, e.g. in Tibet (Williams et al. 2004; Hou et al. 2006) and the Anatolian-Armenian-Iranian plateau (Jackson et al. 1995; Neill et al. 2015), has become as important as studies of rift-related settings to understand alkaline magma genesis.

The exact mechanisms responsible for magma generation in collisional tectonic settings remain enigmatic. Models include slab break-off (Keskin 2003; van Hunen and Allen 2011; Neill et al. 2015), large-scale delamination or thinning of the lithospheric mantle (Innocenti et al. 1982; Pearce et al. 1990) and small-scale lithospheric detachment driven by convection cells (Kaislaniemi et al. 2014; Neill et al. 2015). Moreover, the source of magmas in compressional regimes and their chemical impact on the crust remains disputed. Processes to generate primary magmas in collision zones may involve melting of thickened lithosphere due to breakdown of hydrous phases at the continental suture (Allen et al. 2013) and melting of deeply-subducted continental crust (Zhao et al. 2013). To explain the alkaline character of the erupted or plutonic igneous rocks, several genetic models and processes have been proposed:

1. Low degrees of partial melting of metasomatized upper mantle (Bodeving et al. 2017; Dawson 1987; Marks et al. 2008).
2. Melting of crustal sources, which could be located in the lower crust and mafic in composition (Smith et al. 1988) or in the middle to upper crust and felsic in composition (Downes 1987; Fitton 1987).
3. Fractional crystallization from alkali basalt parental magmas (Delong et al. 1975; Trumbull et al. 2003), with variable degrees of crustal assimilation (Fitton 1987; Jung et al. 2007; Lan et al. 2011).
4. Fenitisation – a high temperature metasomatic alteration driven by alkali-rich fluids incrementally expelled from alkaline or carbonatitic melts (Sindern and Kramm 2000; Suikkanen and Rämö 2017).

Armenia, landlocked between the Black Sea and the Caspian Sea, forms part of the Anatolian-Armenian-Iranian Plateau and is characterised by widespread Cenozoic

volcano-magmatic activity, starting in the Eocene at ~50 Ma and intermittently lasting into the Holocene and historical times (Karakhanian et al. 2002; Moritz et al. 2016; Fig. 1a). Several studies focused on Quaternary volcanic cones on the Anatolian-Armenian-Iranian plateau (Innocenti et al. 1982; Pearce et al. 1990; Keskin et al. 1998), including in the Armenian segments of the Lesser Caucasus mountain range (Karapetian et al. 2001; Karakhanian et al. 2002), and the Miocene/Pliocene magmatic evolution of the region (Dilek et al. 2010; Neill et al. 2013; Kheirkhah et al. 2015). However, investigating the much less studied Paleogene igneous rocks is important to gain a more complete understanding of the long-term magmatic and geodynamic evolution in this setting of continuing convergence and to improve our understanding of collision-driven continental magmatism and mantle dynamics (Dilek et al. 2010; van Hunen and Allen 2011; Moritz et al. 2016).

In this study, we use a range of petrological and geochemical methods to describe and interpret the lithological variations of the Tezhsar volcano-intrusive alkaline ring complex (or Tezhsar Alkaline Complex - TAC) in Armenia. We provide a new $^{40}Ar/^{39}Ar$ age and expand on previous petrological and geochemical studies (Abovyan et al. 1981; Kogarko et al. 1995; Meliksetian 1971, 1989) with the aim to achieve a better understanding of TAC petrogenesis and to integrate that into a model of alkaline magma genesis within a setting of continuing plate convergence. We also highlight and discuss the occurrence of cm-sized pseudoleucites in the TAC.

2. Geological history

2.1 Regional tectonic setting

The TAC, located about 55 km north of Yerevan in the Lesser Caucasus, has formed in the Eocene in a setting of general convergence between the Eurasian and Arabian plates

(Fig. 1a). This region was affected by two distinct collisional events and the emplacement of the alkaline magmas of the TAC is crucial to the understanding of the tectono-magmatic evolution of the region.

The TAC is located on basement of the South Armenian Block (SAB), which is a microplate of Gondwanaland origin (Knipper and Khain 1980; Rolland 2017; Sosson et al. 2010). Proterozoic metamorphic basement of the SAB is exposed in the Tsakhkunyats massif (Belov 1968; Aghamalyan 1998). Platform sedimentary cover of the SAB is presented by folded Late Devonian to the Late Triassic sedimentary formations (Arakelyan 1964; Aslanyan 1958). Ophiolites representing Jurassic oceanic crust were obducted onto the northern margin of the SAB in the Late Cretaceous (90-84 Ma; Rolland 2017). In the late Cretaceous to early Palaeogene (70-60 Ma), the SAB was welded to the southern margin of Eurasia as a result of the closure of the northern branch of the Neotethys and the termination of subduction (Rolland et al. 2009a, b; Moritz et al. 2016). The collision is marked by the Sevan-Akera suture zone, which is part of the regional northern Neotethys suture (Hässig et al. 2013; Sosson et al. 2010). The closure of the northern Neotethys branch caused a subduction jump towards the south and the accretion of the SAB to the Eurasian margin resulted in formation of a Cretaceous-Eocene flysch basin that overlies the ophiolites (Rolland 2017). At present, the Sevan-Akera suture separates two tectonostratigraphic units, the Southern and Northern Tethyan Provinces, which outline the continental provinces pre-dating the closure of the Tethys Ocean (Fig. 1b; Adamia et al. 2011). The Sevan-Akera suture is located ~6 km northward of the TAC. The second stage of accretion involving collision of the Arabian margin to the SAB and the Tauride-Anatolian block caused the closure of the South Neotethys ocean along the Bitlis-Zagros suture. This closure occurred in late Eocene to early Oligocene times (40-25 Ma) based on geochronological and structural evidence (Agard et al. 2005;

157 Allen and Armstrong 2008; Rolland 2017). The convergence and collision between Arabia
158 and Eurasia induced regional compression and shortening in the overriding (SAB-
159 Eurasia) continental lithosphere (Agard et al. 2011), the formation of the Anatolian-
160 Armenian-Iranian orogenic plateau (Sheth et al. 2015) and lateral ejection of the
161 Anatolian and Iranian blocks, with the Armenian Highland (Lesser Caucasus and Eastern
162 Anatolia) in the centre (Phillip et al. 1989). Protracted Cenozoic magmatism lasted from
163 ~49 Ma to ~21 Ma and marked the final stages of the Neothethyan subduction, the main
164 Arabia-Eurasia collisions and subsequent post-collisional events, including emplacement
165 of the syn-collisional granite-leucogranite plutons of the Lesser Caucasus (Meliksetian
166 1989; Rezeau et al. 2017).

167 To explain the Palaeogene magmatism of the entire region, Dilek et al. (2010)
168 proposed the opening of an asthenospheric window beneath the arc mantle wedge and
169 the collision zone. The presence of adakites of Early Eocene age in the Pontides
170 interpreted as a result of slab window formation (Eyuboglu et al. 2011) supports this
171 hypothesis. Lordkipanidze et al. (1989) and Sahakyan et al. (2016) consider a subduction-
172 modified upper mantle source for Lower-Middle Eocene volcanism and an increase of
173 crustal input within the Late Eocene-Early Oligocene magmatic series of the Lesser
174 Caucasus.

175 Considering the age and location of the TAC ($^{40}Ar/^{39}Ar$ of 41.0±0.5 Ma, this study;
176 36.3-37.5 Ma, K-Ar, Baghdasaryan and Ghukasyan 1985; 36-39 Ma, K-Ar, Meliksetian
177 1989), it formed in a plate convergence setting, in between two major collisional events
178 that occurred in region – first at the northern edge of the SAB in the Late Cretaceous to
179 Early Paleogene, and subsequently to the south of the SAB in the Late Eocene to Early
180 Oligocene. The TAC can thus be described as post-collisional relative to the initial
181 collisional event between the SAB and the Eurasian plate.

2.2 Geological setting of the Tezhsar Alkaline Complex

The TAC is located on the Pambak ridge at the northern edge of the SAB within the Sevan-Shirak basin. To the south, the TAC is in contact with the Proterozoic metamorphic basement of the SAB across the Marmarik Fault. Presence of abundant xenoliths from the Tsakhkunyats basement, such as mica schists, confirms the affinity of the TAC to the SAB continental terrane. To the north, the TAC borders the Margahovit intrusion comprising porphyritic granosyenites. Country rocks exposed to the W-NW of the TAC comprise Upper Cretaceous clastic and carbonate strata and Mid-to-Late Eocene extrusive igneous rocks, which also outcrop to the E-SE. The Ulashik Fault cuts the TAC in SW-NE direction with horizontal left-lateral displacement of intrusive and volcanic units reaching 700 m.

The TAC represents a ring complex that can be subdivided into several concentric units of both volcanic and plutonic rocks. Such classical ring complexes are quite rare (Johnson et al., 1999) and are of special interest considering their structural and volcanological evolution as well as petrological aspects. According to Meliksetian (1971), the TAC includes the following major units (Fig. 2):

1. Outer cone sheets characterized by inward-dipping contacts
2. Ring unit of volcanic alkaline rocks with a thickness up to 600 m characterised by its concentric structure and inward-dipping contacts (Outer Volcanic Unit, OVU)
3. Central intrusive unit comprising syenites and nepheline syenites (Syenitic Unit, SYU)
4. Ring dykes, circular bodies with sub-vertical contacts cutting both the volcanic and central intrusive units
5. Resurgent volcanic unit, inside the central intrusive unit, formed by volcanic breccias, dykes and subvolcanic rocks (Central Volcanic Unit, CVU).

For the purpose of the geochemical investigation in this study, we use a simplified subdivision into Outer Volcanic Unit, Syenitic Unit and Central Volcanic Unit (Fig. 2). Based on a structural analysis including bedding attitudes of units and relationships between volcanic ring, cone sheets and central pluton, the presence of circular dykes and remains of a volcanic centre, most researchers, namely Kotlyar (1958), Bagdasaryan (1966) and Meliksetian (1971) concluded that the TAC formed via a caldera collapse and the volcanic ring was emplaced through collapse along concentric faults. The exceptionally large elliptical palaeocaldera structure of the TAC is ~13.6×11.5 km in size and has an area of ~131 km^2, comparable in dimensions to the Santorini caldera in the Aegean Sea. Such a ring morphology provides a unique insight into the roots of an alkaline volcano-plutonic complex.

Beyond the petrogenetic and structural significance of the TAC, there is also a characteristic widespread development of pseudomorphs after leucite, which have been studied in detail by B. Meliksetian (1970, 1971, 1979, 1989) and Yagi and Gupta (1978). They feature in volcanic, subvolcanic and intrusive alkaline rocks and the largest crystals, reaching up to 8 cm in size (Fig. 3) are found in porphyry tinguaite dykes (Meliksetian 1978; Yagi and Gupta 1978). Their crystallographic habit is either icositetrahedral (in volcanic rocks and dykes) or triakis octahedral (in intrusive syenites). In the Soviet petrological literature according to Zavaricky (1934), pseudomorphism after leucite is divided into two mineralogical and genetic types: “Pseudoleucites” referring to leucite breakdown into nepheline and orthoclase, and “epileucites” describing pseudomorphism after leucite composed of agglomerated orthoclase, muscovite, analcime, chlorite, calcite and zeolites. In the Western petrological literature, usually both types are referred to as pseudoleucites, and both types have been described in the TAC.

3. Field observations

Field campaigns in the TAC were carried out in 2008, 2012 and 2015 in order to achieve two major aims: i) Help the completion of geological map (incl. GIS database) of the complex; ii) sampling the various lithologies of the TAC for petrological and geochemical investigations (Fig. 2). Sampling was focused on the three major units generalised for the purposes of this study: The Outer Volcanic Unit (OVU), the inner Syenitic Unit (SYU) and the Central Volcanic Unit (CVU) (Fig. 2), which have been juxtaposed by ring faulting. In total, 46 samples were collected and analysed, and one of those (sample 6-8-12 from the SYU) was used for $^{40}Ar/^{39}Ar$ age determination. Field relations demonstrate that the syenitic magmas of the SYU intruded into the OVU (Fig. 3a). More localized and subordinate lithologies of the complex include syenitic pegmatites (Fig. 3b) and pseudoleucite-bearing phonolites (Fig. 3c-f).

4. Petrography

The pioneering works of Meliksetian (1989) identified >50 different mineral species in rocks of the TAC, including a variety of rare earth element (REE) and high field strength element (HFSE) bearing phases. In our study, we focus on the major rock-forming minerals in the three major rock units of the complex to provide a general overview of the lithologies.

The volcanic rocks of the Outer Volcanic Unit (OVU) are typically porphyritic with an aphanitic groundmass. Major minerals are plagioclase + clinopyroxene + amphibole + biotite + alkali feldspar + Fe-Ti oxides ± nepheline, and apatite and titanite are present as accessory phases. Plagioclase is euhedral to subhedral, weakly zoned and often shows sieve textures (Fig. 4a). Euhedral clinopyroxene phenocrysts are up to 2 mm in size and typically poikilitic. Volcanic breccias are observed occasionally, containing angular

fragments and xenoliths, the latter partly rich in quartz. Volumetrically small occurrences of altered pseudoleucite phonolites are present, where we found pseudomorphed leucite up to several cm in diameter. The deltoidal icositetrahedral crystal habit of the primary leucite is well preserved, but leucite has been completely replaced by secondary minerals. These are dominated by alkali feldspar and cancrinite-group minerals and comprise minor amounts of analcime. Other phases found in the pseudoleucite are clinopyroxene, biotite, apatite and calcite.

The volcanic rocks of the Central Volcanic Unit (CVU) are generally porphyritic with a fine-grained matrix. They contain euhedral plagioclase + alkali feldspar + clinopyroxene + amphibole + biotite + Fe-Ti oxides as major mineral phases. Some samples contain amphibole glomerocrysts and clinopyroxene overgrowing biotite (Fig. 4b). Rare pseudoleucite phonolites occur in this unit as well. The samples of the CVU are often intensely altered.

The Syenitic Unit (SYU) comprises equigranular, phaneritic, medium to coarse-grained syenites and nepheline syenites (Fig. 4c-h). Several samples show a trachytoidal preferential alignment of feldspars. Major mineral phases are alkali feldspar + amphibole + biotite + clinopyroxene + Fe-Ti oxides ± nepheline ± plagioclase. Garnet is rare but very prominent in the coarse grained (pegmatitic) rock varieties, where euhedral to subhedral brown garnet forms clusters with euhedral, black todark green amphibole. Accessory phases observed include zircon, titanite, fluorite, muscovite, apatite, calcite, sodalite and cancrinite. Subhedral alkali feldspar is typically the most abundant phase, frequently exhibiting significant alteration. Primary clinopyroxene commonly shows signs of incipient alteration to green amphibole.

5. Analytical methods

Major and trace elements were analysed by standard X-ray fluorescence (XRF), inductively coupled plasma atomic emission spectrometry (ICP-AES) and inductively coupled plasma mass spectrometry (ICP-MS) methods. Detailed information about the analytical methods used is provided in the supplementary material. Systematic differences between analyses from different laboratories are not observed. If they exist, they are likely to be small relative to the compositional effects of the magmatic processes operating, and considered negligible for the overall interpretation of the dataset.

Strontium (Sr) and neodymium (Nd) isotope analyses were performed at the School of Earth and Environment, University of Leeds. Conventional ion-exchange chromatographic techniques were applied and samples were analyzed on a Thermo Finnigan Triton multicollector mass spectrometer (see Halama et al. 2013 for details of the analytical protocol). Information about reference materials analysed as well as normalization and correction procedures applied is given in the supplementary material.

$^{40}Ar/^{39}Ar$ dating of amphibole from syenite sample 6-8-12 was performed using a CO_2 laser stepwise heating technique at the Institute of Earth and Environmental Science, Universität Potsdam. The analytical protocol follows established procedures and a brief summary about procedural aspects, standards used and corrections applied is provided in the supplementary material. Calculation of ages and errors was performed following Uto et al. (1997) using the total ^{40}K decay constant of 5.543×10^{-10} a^{-1}.

6. Results

6. 1. Rock classification and major element geochemistry

The Total Alkali versus Silica (TAS) diagram was used to classify the volcanic rocks from the OVU and CVU (Fig. 5a). For the intrusive rocks of the SYU, we used the classification diagram of De La Roche et al. (1980; Fig. 5b). Whole rock geochemical

analyses are presented in Table 1. All volcanic rocks of the TAC are classified as alkaline in the TAS diagram (Fig. 5a). Rocks of the OVU cover a wide compositional range from basaltic trachyandesite to phonotephrite, tephriphonolite and phonolite. The compositional range of the CVU rocks is more restricted, comprising trachyandesites and trachytes. The plutonic rocks of the SYU are classified as nepheline syenites and syenites based on the R1 and R2 parameters (Fig. 5b), which generally agrees with the petrographic observations.

A further geochemical classification was carried out using various geochemical indices (Table 1) that allow an evaluation of petrogenetic relationships (Shand 1947; Frost et al. 2001; Frost and Frost 2008). The majority of the Tezhsar rocks are ferroan, alkalic, metaluminous and silica-undersaturated. The Alkalinity Index (AI; AI = Al-(K+Na) on a molecular basis) typically varies between 0 and 0.1, indicating that peralkaline rocks (AI<0) are largely absent at the TAC. Values for the feldspathoid silica-saturation index (FSSI; normative Q-[Lc+2(Ne+Kp)]/100, where Q = quartz, Lc = leucite, Ne = nepheline and Kp = Kaliophilite) mostly range from -0.6 to 0. The negative FSSI values demonstrate that the rocks are generally silica-undersaturated. Diagrams using the aluminium-saturation index (ASI; molecular Al/(Ca-1.67P+Na+K) and the modified alkali-lime index (MALI; Na_2O+K_2O-CaO) classification demonstrate the predominantly metaluminous and alkalic nature of the TAC rocks (Fig. 5c, d). Peraluminous compositions (ASI>1) are very rare. Compared to the restricted compositions of SYU and CVU, the OVU shows the largest variations in A/NK ratios.

Harker diagrams show a relatively smooth decrease of MgO, total FeO (FeO_T) and CaO with increasing SiO_2 contents (Fig. 6a-c). MgO contents are below 3 wt% for OVU rocks and SYU and CVU rocks have less than 1wt% MgO, demonstrating their highly evolved

character and suggesting substantial fractionation of mafic minerals prior to crystallisation.

6.2. Trace element geochemistry

Whole-rock trace element concentrations in the TAC are variable and show some significant enrichment in Sr (up to ~5000 ppm), Ba (up to ~4000 ppm), Zr (up to ~1000 ppm) and ΣREE (up to ~1200 ppm), which is typical for alkaline igneous rocks (Chakhmouradian and Zaitsev 2012). Incompatible trace elements such as Th and Zr show pronounced enrichment with increasing silica, in particular evident for SYU and CVU rocks (Fig. 6d, e). In contrast, Sr contents remain relatively constant for intermediate rocks with <58 wt% SiO_2 and diminishing at higher silica contents (Fig. 6f). A chondrite-normalised REE diagram (Fig. 7a) shows that both the volcanic and plutonic rocks of the TAC are characterised by a strong fractionation between LREE and HREE with $La_{(N)}/Yb_{(N)}$ ratios predominantly around 10-40 but reaching values as high as 70. Absolute amounts of LREE are generally higher in the SYU (~200-1000 x chondrite) compared to the OVU and CVU (~40-500 x chondrite). Europium anomalies, defined as $Eu/Eu^*=\frac{Eu_N}{\sqrt{(Sm_N \times Gd_N)}}$, are moderately negative in the volcanic units OVU (0.80 – 1.08) and CVU (0.68 - 0.91). The majority of the SYU rocks have more pronounced negative Eu anomalies with Eu/Eu* values between 0.44 and 0.97 (Fig. 7a). On primitive mantle-normalised trace element diagrams (Fig. 7b-d), negative anomalies for Nb, Ta and Ti are the most prominent features in all three units. In contrast, a strong relative enrichment of Th and U compared to Rb and Ba is only significant in the SYU and CVU, but not discernible in the OVU.

6.3 Sr and Nd isotopes

Initial Sr and Nd isotope ratios of volcanic and plutonic rocks from the TAC,

recalculated to an age of 41 Ma, range from 0.7040 to 0.7052 and 0.51274 to 0.51283, respectively (Table 1). 19 of 20 samples fall within the range 0.7040 to 0.7044 for the initial $^{87}Sr/^{86}Sr$ ratio. The Nd isotopic compositions correspond to positive εNd values between +3.0 and +4.8 (Table 1).

6.4 $^{40}Ar/^{39}Ar$ geochronology

One syenite sample (sample number 6-8-12) was dated by $^{40}Ar/^{39}Ar$ step heating. The total gas age is 42.1 ± 0.5 Ma (Fig. 8; Table 2). We use the following criteria outlined by Fleck et al. (1977) for defining a plateau age: (1) The plateau includes at least 50% of the total ^{39}Ar released, (2) the ages of two contiguous steps in the plateau agree within 2s error, excluding the J value error, (3) the plateau consists of three steps or more, and (4) each degassing step contributing to the plateau contains >3% of the total ^{39}Ar released. For the syenite sample 6-8-12, five plateau steps constituting 98.88% of the total ^{39}Ar released can thus be used to define a plateau age of 41.0 ± 0.5 Ma (Fig. 8; Table 2). Using the plateau steps only, a normal isochron age of 41.3 ± 2.5 Ma with a $^{40}Ar/^{36}Ar$ intercept at 281 ± 58 is obtained. The corresponding inverse isochron yields an age of 41.2 ± 2.1 Ma with $(^{40}Ar/^{36}Ar)_i$ = 289 ± 57. The good agreement between the three ages underlines the reliability of the age determination, with the plateau age of 41.0 ± 0.5 Ma representing the most precise and hence preferred age.

7. Discussion

7.1 Comparison with regional magmatic signatures

The alkaline and highly evolved nature of the TAC rocks makes them distinct from volcanic rocks outcropping in Armenia, which are typically transitional between alkaline and subalkaline. This includes the trachybasaltic to trachyandesitic Pliocene-Quaternary

rocks from northern Armenia (Neill et al. 2013, 2015), as well as rocks from the large polygenetic Aragats volcano (Connor et al., 2011) and from the Gegham, Vardenis and Syunik Volcanic Highlands in South Armenia (Karapetian et al. 2001; Sugden et al. submitted). A comparison with data for regionally related Miocene to Quaternary Armenian igneous rocks from the Yerevan and Shirak regions (Neill et al. 2015) reveals a general enrichment of the TAC rocks in almost all moderately to highly incompatible trace elements (Fig. 7b-d). Key features, such as negative Nb-Ta and Ti anomalies and a relative enrichment of LREE compared to HREE, are similar. Isotopically, the TAC rocks, which plot on the Sr-Nd mantle array, overlap with plutonic rocks from the Meghri-Ordubad pluton and with other Miocene to Quaternary volcanic rocks from Armenia (Fig. 9). Quaternary volcanic rocks from Aragats (Lebedev et al. 2007; Connor et al. 2011) and the Gegham Ridge (Lebedev et al. 2013) also overlap in their Sr-Nd isotopic compositions. This comparison reveals that there is a broad Sr-Nd isotopic homogeneity across a large area of the Armenian highlands from the Eocene to the Quaternary, indicating that similar source regions are involved in magma genesis. Broadly contemporary (47-40 Ma) post-collisional magmatic rocks from the Eastern Pontides (NE Turkey), which are characterized by tholeiitic/calc-alkaline affinities enriched in LILE with pronounced depletions in HFSE, also overlap in their isotopic composition (Aydınçakır & Şen 2013). In contrast, extending the comparison to Eocene magmatic rocks in NW Iran reveals that post-collisional granites and syenites from the Sanandaj-Sirjan Zone and granitoids from the Urumieh-Dokhtar magmatic arc extend to significantly more radiogenic Sr-Nd isotope compositions (Fig. 9).

7.2. Magma differentiation and magma source geochemistry

Both volcanic and plutonic rocks of the TAC are evolved and only a few samples are

406 of intermediate composition (Fig. 5a, b). The influence of mixing, fractional crystallization
407 and batch partial melting on the bulk geochemical composition of the rocks can be
408 evaluated using incompatible trace elements with different bulk solid/liquid partition
409 coefficients (Schiano et al. 2010). In the Rb/Nd vs. Rb diagram (Fig. 10a), the near-
410 horizontal trend for the majority of data points emphasizes the dominant role of fractional
411 crystallization, whereas mixing and differences in batch partial melting would yield
412 positive correlations (Schiano et al. 2010). This interpretation is supported by a curved
413 overall trend in the Rb vs. Rb/V diagram (Fig. 10b), which is consistent with fractional
414 crystallisation or mixing, but not with different degrees of partial melting (Schiano et al.
415 2010). Moreover, the coherent trend of the Rb/Ba vs. Ba diagram (Fig. 10c) reflects
416 feldspar fractionation and does not indicate any significant effects of hydrothermal
417 alteration. A major role of role of crustal contamination processes can also be excluded
418 based on the unradiogenic initial $^{87}Sr/^{86}Sr$ isotope ratios that remain relatively constant
419 with increasing silica (Fig. 10d). Crustal contamination typically leads to an coupled
420 increase in $(^{87}Sr/^{86}Sr)_i$ and SiO_2, which is not observed for the TAC. The only sample with
421 an elevated $(^{87}Sr/^{86}Sr)_i$ ratio (2-7-09) has a high Rb/Sr ratio of ~8 and might be affected
422 by a larger uncertainty in recalculation of the initial value and/or post-magmatic Rb or Sr
423 mobilization. There is also no indication of limestone assimilation, which would lead to a
424 significant enrichment in CaO (Fig. 6c).
425 Olivine is conspicuously absent in all TAC rocks, but the low MgO contents and the
426 highly evolved character point to preceding fractionation of mafic minerals (Fig. 6). The
427 decrease in CaO/Al_2O_3 coupled with increasing FeO_t/MgO ratios, Eu anomalies that
428 become more negative with increasing degree of differentiation, and decreasing Sr
429 contents and Dy/Yb ratios with increasing SiO_2 suggest a significant role of
430 amphibole/clinopyroxene and plagioclase fractionation whereas garnet fractionation

was insignificant (Fig. 11a-c). Typically, the OVU rocks are more primitive than both CVU and SYU rocks. OVU rocks even retain Eu/Eu* values close to 1, pointing to lack of significant plagioclase fractionation (Fig. 11b).

The pronounced depletions in HFSE (Nb, Ta, and Ti) in all TAC rocks emphasizes the influence of subduction processes on the mantle source (Fig. 7). Similar negative HFSE anomalies have been observed in alkaline rocks of the Longbaoshan Complex, North China Craton (Lan et al. 2011) and carbonatites from east Tibet in the Himalayan collision zone (Hou et al. 2006) and were attributed to subduction processes influencing the magma source regions prior to continental collision. In addition, various trace element indicators for source enrichment processes support the notion that the OVU and the CVU are geochemically distinct (Fig. 11d-f). The OVU shows elevated Sm/Yb and Ba/La ratios, as well as relatively low La/Sm and Th/Yb ratios compared to the CVU (Fig. 11d-f). Collectively, these geochemical features of the OVU are interpreted as a signature of moderate fluid enrichment via slab dehydration inherited from earlier subduction events. Both CVU and OVU rocks share high Ba/Nb ratios, similar to arc volcanic rocks in general (Fig. 12a). There is little overlap between the two groups as OVU rocks are additionally characterized by, on average, higher La/Nb ratios and Ba/Nb ratios >100, suggesting a temporal evolution towards a decreasing subduction influence from the early OVU to the late stage CVU. The more scattered trend towards lower Ba/Nb ratios in the syenites and nepheline syenites is likely a result of progressive alkali feldspar fractionation and should not be considered as the parental magma signature. The felsic plutonic rocks from the SYU tend to exhibit a larger geochemical variability when compared with the volcanic rocks, which is likely related to the fact that some show cumulate textures and may not represent melt compositions. The CVU, in contrast, has compositions that are more tightly clustered, with a faint indication of source enrichment from subducted sediments.

456 Mechanisms of enrichment of the mantle source can be distinguished using $[Hf/Sm]_N$ and
457 $[Ta/La]_N$ ratios (Fig. 12b), where TAC rocks are characterized by a subduction
458 metasomatism signature, clearly distinct from carbonatitic metasomatism.
459 Sr-Nd isotopic compositions are broadly overlapping with Eocene to Pliocene
460 magmas from the Meghri-Ordubad pluton and Pliocene to Quaternary volcanism in
461 central and northern Armenia, pointing to only minor spatial variations in the respective
462 mantle source regions (Fig. 10). The source of the TAC magmas is dominated by a depleted
463 mantle component and crustal contamination is essentially absent, as all of the possible
464 crustal contaminants would greatly enhance the radiogenic isotope signatures of the
465 magmas, which is not the case. Silica-undersaturated alkaline rocks commonly have
466 isotopic compositions that suggest a magma source in the mantle (Dunworth and Bell
467 2001; Kramm and Kogarko 1994). For instance, nepheline syenites from the Gardar
468 Province (Greenland) show Nd isotopic compositions typical for mantle-derived rocks
469 without any significant crustal assimilation (Halama et al. 2005; Marks et al. 2004).
470 Therefore, evolved silica-undersaturated rocks are interpreted as products of
471 differentiation from more primitive nephelinitic, basanitic or alkali basaltic magmas
472 derived from the upper mantle (Kramm and Kogarko 1994; Trumbull et al. 2003).
473 Basanitic volcanism is common to the south of TAC in the Syunik Volcanic Highland
474 (Sugden et al. submitted) near the Armenia-Azerbaijan-Iran border region.
475 The trace element evidence for a subduction modifications and the Sr-Nd isotopic
476 evidence for previous melt extraction suggest that the TAC magmas are predominantly
477 derived by low degrees of partial melting from a lithospheric mantle source which has
478 been affected by pre-Eocene subduction i.e., prior to post-collisional melt generation. This
479 magma generation model is also the preferred model for volcanism in East Anatolia
480 (Keskin 2003), and similar geochemical features in volcanic rocks from the Eastern

Pontides (Artvin Province) contemporary (47-40 Ma) to emplacement of the TAC were also interpreted to be derived from a mantle source that had experienced metasomatism by slab-derived fluids (Aydınçakır & Şen 2013). Post-collisional magmatic processes are commonly affected by prior subduction processes and LILE-enriched mantle sources are characteristic for these rocks (Bonin et al. 1998), typically resulting in calc-alkaline magmatic suites (Harris et al. 1986). The TAC represents an unusual case insofar as the post-collisional magmatic rocks are alkaline in character but also derive from a subduction-modified mantle source.

7.3. The age of the Tezhsar Alkaline Complex in a regional context

The mid-Eocene age of 41.0 ± 0.5 Ma falls into a time of widespread magmatism in the Lesser Caucasus region, which lasted from ~49 to ~38 Ma and comprised the emplacement of alkaline and nepheline-bearing gabbros, monzonites and syenites as well as gabbro-diorite-granodiorite-syenogranite complexes and granites (Ghukasyan et al. 2006; Melkonyan et al. 2008; Moritz et al. 2016). The magmatic activity was accompanied by porphyry-type Cu-Mo mineralization that was dated at 44-40 Ma by Re-Os analyses of molybdenite (Moritz et al. 2016). Slightly younger alkaline magmatism is represented by the Bunduk alkaline complex (38-32 Ma) located ~15 km northeast of the TAC (Abovyan et al., 1981; Meliksetian, 1989). This pluton intrudes the Middle-Late Eocene volcanic suite of the Bazum ridge and the Bazum gabbro-granitoid intrusive complex, exhibiting an elongate morphology, parallel to the segment of Pambak-Sevan fault.

Regionally, broadly contemporaneous magmatic activity is also recorded in the Talysh mountain range (Azerbaijan/Iran) at around 41-38 Ma (Vincent et al. 2005), in the Eastern Pontides (Turkey) at ~46-40 Ma (Aydınçakır and Şen 2013) and in western Georgia at ~47-41 Ma (Lebedev et al. 2009). Further to the SE in the Zagros orogen, ~41

506 Ma old granites and syenites occur in the Piranshahr massif (Mazhari et al. 2009) and ~40
507 Ma granitoids in the Urumieh-Dokhtar arc (Kazemi et al. 2018). The peak of subduction-
508 related magmatism in Iran is also close to 40 Ma (Allen and Armstrong 2008), and a
509 magmatic flare-up lasting ~18 million years from 55 to 37 Ma has been postulated in the
510 Urumieh-Dokhtar belt and the Alborz Mountains in Iran (Verdel et al. 2011). Throughout
511 the Eocene, the plate convergence between the Arabian and Eurasian plates was
512 proceeding at rates of 2-3 cm/year (McQuarrie et al. 2003). Following the initiation of the
513 Arabia-Eurasia collision, arc magmatism declined in the Late Eocene (Allen and
514 Armstrong 2008). However, convergence was relatively rapid throughout Eocene-
515 Oligocene time, and only slowed since Early Miocene (Rosenbaum et al. 2002).

516 The age of the TAC falls within this period of extensive magmatism during
517 convergence between the Arabian and Eurasian plates, and its geochemical
518 characteristics demonstrate a subduction-related origin. This subduction signature is
519 inherited from prior northward subduction of the Neotethys ocean underneath the
520 Eurasian margin, leading to a preconditioning of the mantle (Verdel et al. 2011). Typical
521 calc-alkaline, subduction-related Eocene magmatism typical for active arc environments
522 is preserved in the oldest granitoids (49-44 Ma) of the Meghri-Ordubad pluton (Moritz et
523 al. 2016). The Lesser Caucasus experienced extension and crustal thinning at around 40
524 Ma causing decompression melting of the hydrated, subduction-influenced lithospheric
525 mantle (Verdel et al. 2011), which imparted its geochemical signature onto the TAC
526 magmas. Middle Eocene (ca. 49–40 Ma) extension, accompanied by magmatism, also
527 occurred in Iran (Ballato et al. 2011). The extension-related magmatism in an overall
528 setting of convergence (Rosenbaum et al. 2002) is caused by the rollback of the Neotethys
529 slab (Vincent et al. 2005; Verdel et al. 2011).

530 The oldest rocks at TAC in the OVU show some geochemical characteristics
531 reminiscent of a dehydration fluid signature in arc magmatic rocks (high Ba/Nb, Ba/La
532 ratios; Figs. 7 and 11e, f). A clear arc signature, most evident in the pronounced negative
533 Nb-Ta anomalies, is present in all of the TAC rocks, similar to the Meghri-Ordubad pluton
534 at the Armenia-Iran border. However, the TAC rock compositions are distinct as they are
535 not calc-alkaline but alkaline (Fig. 5) with a pronounced enrichment in incompatible trace
536 elements (e.g. up to 5000 ppm Sr and typically 100-500 ppm Rb compared to <1000 ppm
537 Sr and 10-200 ppm Rb in rocks from Meghri). This geochemical character is not due to
538 long-lived differences in the mantle source compared to Meghri-Ordubad pluton since the
539 Sr-Nd isotopic characteristics are similar (Fig. 9). Instead, smaller degrees of melting
540 and/or a metasomatic enrichment episode(s) immediately prior to magma generation
541 have to be invoked. The very pronounced subduction signature in the TAC supports the
542 predominant melting of hydrated and HFSE-depleted lithospheric mantle, with
543 subordinate contributions from upwelling astenospheric mantle (Verdel et al. 2011). The
544 occurrence of these alkaline rocks in a general setting of convergence is unusual, but can
545 be attributed to periods of localized extension in the Lesser Caucasus. The overall
546 convergence throughout Eocene and Oligocene is well established based on kinematic
547 data and modelling (Rosenbaum et al. 2002), but if the lithospheric structures allowed
548 ascent of mantle-derived magmas via localized faulting and/or rift tectonics alkaline
549 magmatism can develop even in collision zones (Harris et al. 1986). Development of an
550 extensional regime along this sector of Lesser Caucasus was previously suggested to
551 explain the alkaline character of Paleogene magmatic rocks, particularly those within
552 Armenia (Kogarko et al., 1995).
553
554 **7.4. Petrogenesis of pseudoleucite phonolites**

555 Based on optical microscopy and geochemical analyses including XRD, 6 types of
556 “epileucites” and 5 types of pseudoleucites were distinguished by their mineral
557 associations, host rocks and crystallographic habit (Meliksetian 1971, 1978). “Epileucites”
558 are considered to be a result of post-magmatic hydrothermal alterations, whereas
559 pseudoleucites are considered to be a result of disintegration of metastable K-Na leucite
560 into mixture of orthoclase and nepheline under subsolidus conditions (T=600°C) in late
561 magmatic stage (Meliksetian 1978; Gittins et al. 1980). Yagi and Gupta (1978) mention
562 that the K_2O/Na_2O ratio of 4.3 in pseudoleucites of porphyry tinguaite dykes of TAC is the
563 highest among those studied worldwide highlighting the importance of resolving
564 complex’s evolutionary story to better understand the conditions of pseudoleucite
565 paragenesis.

566 The investigated leucite pseudomorphs occur in a phonolite (Fig. 3c-f). Relicts of
567 primary leucite are lacking, and they are generally rarely observed in leucite
568 pseudomorphs. The leucite pseudomorphs mainly consist of alkali feldspar but do not
569 contain nepheline, instead comprising abundant cancrinite (Fig. 13b-c). Different theories
570 about the genesis of leucite pseudomorphs were put forward (see Edgar, 1984, and
571 references therein), including (1) subsolidus breakdown of leucite to orthoclase and
572 nepheline, (2) reaction of leucite with a Na-rich liquid and (3) alkali ion exchange
573 reactions between leucites and Na-rich glass or fluid. We will briefly discuss these
574 theories in relation to the leucite pseudomorphs in the phonolite.

575 Subsolidus breakdown of common K-rich leucite would produce alkali feldspar and
576 kalsilite, hence a process to cause relative enrichment of Na is required to explain the
577 occurrence of Na-bearing phases in pseudoleucites. Leucite solid solutions with up to 40
578 wt.% $NaAlSi_2O_6$ were produced experimentally, and these experienced subsequent
579 breakdown into nepheline and alkali feldspar (Fudali 1963). However, natural leucite

580 does not contain excess amount of sodium to form this type of intergrowth on
581 decomposition (Viladkar 2010). The mineralogy of the leucite pseudomorph, comprising
582 abundant Na-bearing phases such as cancrinite and analcime (Fig. 13b-c), suggest that
583 they are derived from a Na-rich precursor phase. Hence, subsolidus breakdown of natural
584 K-rich leucite alone cannot explain their occurrence, but formation of a metastable Na-
585 rich leucite before breakdown might be possible (Taylor and MacKenzie 1975).
586 The pseudoleucite reaction is a reaction of leucite with a Na-rich magma to form alkali
587 feldspar and nepheline in the system $NaAlSiO_4$ – $KAlSiO_4$ – SiO_2 (Bowen and Ellestad 1937;
588 Edgar 1984). This reaction terminates the leucite stability field and leucite disappears by
589 reaction with the magma (Bowen and Ellestad 1937). The TAC leucite pseudomorphs,
590 however, are characterized by a well-preserved deltoidal icositetrahedral crystal habit,
591 reflecting the external shape of the precursor phase. It is difficult to envisage this reaction
592 to fully replace primary leucite without modifying the morphology of the leucites (Taylor
593 and MacKenzie 1975), which is so beautifully preserved (Fig. 3). Moreover, various minor
594 mineral phases that contain additional elements occur within the pseudomorphs. Some
595 of these (e.g. clinopyroxene, apatite) may be explained as primary magmatic inclusions,
596 but others (analcime, calcite) texturally appear as secondary phases (Fig. 13b-c). This
597 suggests that explaining the genesis of the leucite pseudomorphs based on the phase
598 relations in this petrogenetic system is an oversimplification (Edgar 1984).
599 Alkali ion exchange reactions between leucites and Na-rich glass or fluid was
600 proposed as mechanism to produce pseudomorphs after leucite that are similar in
601 composition to natural pseudoleucites (Taylor and MacKenzie 1975). Fluid-induced
602 reactions would facilitate the increase in Na content and formation of Na-dominated
603 phases, such as cancrinite and analcime in TAC. Cancrinite is assumed to replace
604 nepheline due to a reaction between nepheline and volatile-rich melts or fluids, a common

605 late magmatic– hydrothermal process (Martins et al. 2017). A reaction with fluids was
606 also used to explain pseudoleucite with intergrowth of alkali feldspar, sericite and
607 cancrinite from the Gardar Province, Greenland (Hesselbo 1986) and the replacement of
608 nepheline by analcime, cancrinite, sodalite and muscovite in pseudoleucite from India
609 (Viladkar 2010). Cancrinite is also an important constituent of the pseudoleucite
610 phenocrysts from Spotted Fawn Creek (Yukon Territory, Canada), where also garnet,
611 biotite, calcite, muscovite and plagioclase occur as inclusions within pseudoleucite
612 (Tempelman-Kluit 1969). Removal of K, addition of Na and water was attributed to the
613 entry of a fluid phase to permit the chemical exchange (Tempelman-Kluit 1969). The
614 presence of cancrinite in the TAC leucite pseudomorphs bears evidence for interaction
615 with a H_2O-CO_2-bearing fluid, possibly with minor amounts of S and Cl, as the general
616 formula for cancrinite is $(Na,Ca,K)_{6-8}Al_{6-x}Si_{6+x}O_{24}(CO_3,SO_4,Cl,OH)_{1-2}\cdot nH_2O$ with $x << 1$ and
617 $n = 1–5$ (Martins et al. 2017) illustrates. Given the scarcity of analcime in the TAC
618 pseudoleucites, a conversion of primary leucites into analcime via reaction with Na-rich
619 fluids as proposed for pseudoleucites from a phonolite dyke in Bohemia (Pivec et al. 2004)
620 seems unlikely. The texture of the TAC leucite pseudomorphs pseudoleucites has
621 resemblance to a “palisade texture”, in which orthoclase laths near the margins of the
622 pseudomorphs are oriented at right angles to the crystal boundaries (Tempelman-Kluit
623 1969). These textures can be interpreted to form by subsolidus reactions in response to
624 increasing fluid pressure when pervasive fluids come in contact with the leucite (Hesselbo
625 1986). All these lines of evidence point to a late/post-magmatic hydrothermal alteration
626 for the formation of the leucite pseudomorphs in the investigated phonolite, and they can
627 be referred to as “epileucites”. Complementary evidence for fluid-rich conditions during
628 the late to post-magmatic evolution of the TAC are the presence of pegmatites and the
629 widespread alteration in the CVU rocks.

8. Conclusions

- A combination of small degrees of partial melting and pre-conditioning of the mantle source by slab dehydration and subsequent metasomatic processes can explain the alkaline, subduction-influenced geochemical character of the TAC.
- The Sr-Nd isotopic data demonstrate a mantle source with negligible crustal influence. There is a broad isotopic overlap with Eocene to Quaternary magmatism in other regions of Armenia, suggesting the regional presence of isotopically similar mantle source regions.
- The emplacement of the syenitic units of the TAC was dated by $^{40}Ar/^{39}Ar$ at 41.0 ± 0.5 Ma. The emplacement of the TAC can thus be linked to a previously proposed model of Eocene Neotethyan slab rollback driving decompression melting and extension-related magmatism in Iran and Azerbaijan within a tectonic setting of general convergence between the Arabian and Eurasian plates.
- The formation of leucite pseudomorphs is related to initial leucite crystallization from an evolved, silica-undersaturated magma followed by subsolidus breakdown and interaction with a late to post-magmatic fluid. The magmatic-hydrothermal fluid percolating through the rocks caused alteration of nepheline into cancrinite and amphibolitisation of clinopyroxenes. This fluid overprint may be responsible for the plethora of REE-bearing phases described previously within the TAC and hence be a crucial factor in the (re)distribution of rare elements in alkaline igneous rocks.

Acknowledgements:

We thank the Armenian Academy of Sciences in Yerevan for logistical support during fieldwork. We also thank U. Westernströer for help with solution ICP-MS analyses in Kiel, A. Musiol for performing REE analyses in Potsdam, D. Wilde and P. Greatbatch for producing thin sections, and S. Whitley for advice on the discussion. V. Lebedev and an anonymous reviewer provided constructive comments that helped to improve the manuscript, and N. Eby is thanked for efficient editorial handling. Financial support through Santander Travel Bursaries to KS and RH for the 2015 field campaign is greatly appreciated.

References:

Abovyan, S.B., Aghamalyan, V.A., Aslanyan, A.T., Magalkyan, I.G. (Eds.), 1981. Magmatic and metamorphic formations of the Armenian SSR. Akademiya Nauk Armyanskoi SSR, Yerevan.

Adamia, S., Zakariadze, G., Chkhotua, T., Sadradze, N., Tsereteli, N., Chabukiani, A., Gventsadze, A., 2011. Geology of the Caucasus: A Review. Turkish Journal of Earth Sciences 20:489-544.

Agard, P., Omrani, L., Jolivet, L., Mouthereau, F., 2005. Convergence history across Zagros (Iran): constraints from collisional and earlier deformation. International Journal of Earth Sciences 94:401-419.

Agard, P., Omrani, J., Jolivet, L., Whitechurch, H., Vrielynck, B., Spakman, W., Monié, P., Meyer, B., Wortel, R., 2011. Zagros orogeny: a subduction-dominated process. Geological

679 Magazine 148:692-725.
680
681 Aghamalyan, V.A., 1998. The crystalline basement of Armenia. Thesis of PhD dissertation,
682 Institute of Geological Sciences of National Academy of Sciences, Yerevan, Armenia (in
683 Russian).
684
685 Allen, M.B., Armstrong, H.A., 2008. Arabia-Eurasia collision and the forcing of mid-
686 Cenozoic global cooling. Palaeogeography, Palaeoclimatology, Palaeoecology 265:52-58.
687
688 Allen, M.B., Kheirkhah, M., Neill, I., Emami, M.H., McLeod, C.L., 2013. Generation of arc and
689 within-plate chemical signatures in collision zone magmatism: Quaternary lavas from
690 Kurdistan Province, Iran. Journal of Petrology 54:887-911.
691
692 Arakelyan, R.A., 1964. The Paleozoic-Mesozoic, in: Geology of the Armenian SSR. Academy
693 of Sciences of the Armenian SSR, Yerevan, pp. 21-163 (in Russian).
694
695 Aslanyan, A.T., 1958. Regional geology of Armenia. Haypetrat, Yerevan (in Russian).
696
697 Aydınçakır, E., Şen, C., 2013. Petrogenesis of the post-collisional volcanic rocks from the
698 Borçka (Artvin) area: Implications for the evolution of the Eocene magmatism in the
699 Eastern Pontides (NE Turkey). Lithos 172-173:98-117.
700
701 Bagdasaryan, G.P., 1966. Intrusive rocks of the Bazum-Pambak region, in: Geology of the
702 Armenian SSR, Intrusive rocks, Academy of Sciences of the Armenian SSR, Yerevan, pp.
703 256-308 (in Russian).

704

705 Bagdasaryan, G.P., Meliksetian, B.M., Ghukasyan, R.Kh., 1985. The alpine gneissic-granitic
706 complex of the Zanguezoor prominence pre-Alpine foundation. Earth Science Letters,
707 Academy of Sciences, Armenian SSR, Yerevan, vol. 38(2), pp. 9-20 (in Russian).

708

709 Ballato, P., Uba, C.E., Landgraf, A., Strecker, M.R., Sudo, M., Stockli, D.F., Friedrich, A.,
710 Tabatabaei, S.H., 2011. Arabia-Eurasia continental collision: Insights from late Tertiary
711 foreland-basin evolution in the Alborz Mountains, northern Iran. Geological Society of
712 America Bulletin 123: 106-131.

713

714 Belov, A.A., 1968. Boundary between Gondwana and Eurasia, and Palaeotethys suture in
715 Caucasian sector of Mediterranean fold belt, in: Tectonics, structural geology, planetology.
716 Works of Soviet geologists, XXV session of IGC, P83.

717

718 Bodeving, S., Williams-Jones, A.E., Swinden, S., 2017. Carbonate-silicate melt immiscibility,
719 REE mineralising fluids, and the evolution of the Lofdal Intrusive Suite, Namibia. Lithos
720 268:383-398.

721

722 Bonin, B., Azzouni-Sekkal, A., Bussy, F., Ferrag, S., 1998. Alkali-calcic and alkaline post-
723 orogenic (PO) granite magmatism: petrologic constraints and geodynamic settings. Lithos
724 45:45-70.

725

726 Boulton, S., 2009. Record of Cenozoic sedimentation from the Amanos Mountains,
727 Southern Turkey: Implications for the inception and evolution of the Arabia-Eurasia
728 continental collision. Sedimentary Geology 216:29-47.

729

730 Bowen, N.L., Ellestad, R.B., 1937. Leucite and pseudoleucite. American Mineralogist
731 22:409-415.

732

733 Burke, K., Khan, S., 2006. Geoinformatic approach to global nepheline syenite and
734 carbonatite distribution: Testing a Wilson cycle model. Geosphere 2:53-60.

735

736 Chakhmouradian, A.R., Zaitsev, A.N., 2012. Rare earth mineralization in igneous rocks:
737 sources and processes. Elements 8:347-353.

738

739 Connor, C., Connor, L., Halama, R., Meliksetian, K., Savov, I., 2011. Volcanic Hazard
740 Assessment of the Armenia Nuclear Power Plant Site, Final Report. Tampa, Leeds, Yerevan.

741

742 Costa, F., Andreastuti, S., Bouvet de Maisonneuve, C., Pallister, J.S., 2013. Petrological
743 insights into the storage conditions, and magmatic processes that yielded the centennial
744 2010 Merapi explosive eruption. Journal of Volcanology and Geothermal Research
745 261:209-235.

746

747 Davidson, J., Turner, S., Handley, H., Macpherson, C., Dosseto, A., 2007. Amphibole "sponge"
748 in arc crust? Geology 35:787-790.

749

750 De La Roche, H., Leterrier, J., Grandclaude, P., Marchal, M., 1980. A classification of volcanic
751 and plutonic rocks using R_1R_2-diagram and major element analyses – its relationships
752 with current nomenclature. Chemical Geology 29:183-210.

753

754 Delong, S.E., Hodges, F., Arculus, R.J., 1975. Ultramafic and mafic inclusions, Kanaga Island,
755 Alaska and the occurrence of Alkaline Rocks in Island Arcs. Journal of Geology 83:721-736.
756
757 DePaolo, D.J., Wasserburg, G.J., 1979. Petrogenetic mixing models and Nd-Sr isotopic
758 patterns. Geochimica et Cosmochimica Acta 43:615-627.
759
760 Dilek, Y., Imamverdiyev, N., Altunkaynak, S., 2010. Geochemistry and tectonics of Cenozoic
761 volcanism in the Lesser Caucasus (Azerbaijan) and the peri-Arabian region: collision-
762 induced mantle dynamics and its magmatic fingerprint. International Geology Reviews
763 52:536-578.
764
765 Downes, H., Balaganskaya, E., Beard, A., Liferovich, R., Demaiffe, D., 2005. Petrogenetic
766 processes in the ultramafic, alkaline and carbonatitic magmatism in the Kola Alkaline
767 Province: A review. Lithos 85:48-75.
768
769 Draper, D.S., Green, T.H., 1997. P-T phase relations of silicic, alkaline, aluminous mantle-
770 xenolith glasses under anhydrous and C-O-H fluid-saturated conditions. Journal of
771 Petrology 38:1187-1224.
772
773 Dunworth, E.A., Bell, K., 2001. The Turiy massif, Kola peninsula, Russia: isotopic and
774 geochemical evidence for a multi-source evolution. Journal of Petrology 42:377-405.
775
776 Edgar, A.D., 1984. Chemistry, occurrence and paragenesis of feldspathoids: A review.
777 NATO ASI Series, series C: Mathematical and Physical Sciences 137:501-532.
778

779 Ewart A., 1982. Petrogenesis of the Tertiary anorogenic volcanic series of Southern
780 Queensland, Australia, in the light of trace element geochemistry and O, Sr and Pb isotopes.
781 Journal of Petrology 23:344-382.
782
783 Eyuboglu, Y.M., Santosh, M., Chung, S-L., 2011. Crystal fractionation of adakitic magmas in
784 the crust-mantle transition zone: Petrology, geochemistry and U-Pb zircon chronology of
785 the Seme adakites, eastern Pontides, NE Turkey. Lithos 121:151-166.
786
787 Fitton J. G., 1987. The Cameroon line, West Africa: a comparison between oceanic and
788 continental alkaline volcanism, in: Fitton, J.G., Upton, B.G.J. (Eds.), Alkaline Igneous Rocks.
789 Geological Society Special Publications 30:273-291.
790
791 Fleck, R.J., Sutter, J.F., Elliot, D.H., 1977. Interpretation of discordant $^{40}Ar/^{39}Ar$ age-spectra
792 of Mesozoic tholeiites from Antarctica. Geochimica et Cosmochimica Acta 41:15-32.
793
794 Fletcher C. J. N., Beddoe-Stephens, 1987. The petrology, chemistry and crystallization
795 history of the Velasco alkaline province, eastern Bolivia, in: Fitton, J.G., Upton, B.G.J. (Eds.),
796 Alkaline Igneous Rocks. Geological Society Special Publications 30:403-413.
797
798 Frost, B.R., Frost, C.D., 2008. A geochemical classification for feldspathic igneous rocks.
799 Journal of Petrology 49:1955-1969.
800
801 Frost, B.R., Arculus, R.J., Barnes, C.G., Collins, W.J., Ellis, D.J., Frost, C.D., 2001. A
802 geochemical classification of granitic rocks. Journal of Petrology 42:2033-2048.
803

804 Fudali, R.F., 1963. Experimental studies bearing on the origin of pseudoleucite and
805 associated problems of alkali rock systems. Geological Society of America Bulletin 74:
806 1101-1126.
807
808 Ghukasyan, R.Kh., Tayan, R.N., Haruntunyan, M.A., 2006. Rb-Sr investigations of magmatic
809 rocks of Kadjaran ore field (Republic of Armenia), in: Isotope dating of processes of ore
810 mineralization, magmatism, sedimentation and metamorphism, Materials of III Russian
811 conference on isotope geochronology I, pp. 213-216.
812
813 Gittins, J., Fawcett, J.J., Brooks, C.K., Rucklidge, J.C., 1980. Intergrowths of nepheline-
814 potassium feldspar and kalsilite-potassium feldspar: A re-examination of the 'pseudo-
815 leucite problem'. Contributions to Mineralogy and Petrology 73:119-126.
816
817 Gupta, A.K., Fyfe, W.S., 1975. Leucite survival: The alteration to analcime. Canadian
818 Mineralogist 13:361-363.
819
820 Halama, R., Savov, I.P, Garbe-Schönberg, D., Schenk, V., Toulkeridis, T., 2013. Vesuvianite
821 in high-pressure-metamorphosed oceanic lithosphere (Raspas Complex, Ecuador) and its
822 role for transport of water and trace elements in subduction zones. European Journal of
823 Mineralogy 25:193–219.
824
825 Halama, R., Vennemann, T., Siebel, W., Markl, G., 2005. The Grønnedal-Ika carbonatite-
826 syenite complex, South Greenland: Carbonatite formation by liquid immiscibility. Journal
827 of Petrology 46:191-217.
828

829 Harris, N.B.W., Pearce, J.A., Tindle, A.G., 1986. Geochemical characteristics of collision-
830 zone magmatism. Geological Society of London Special Publications 19:67-81.
831
832 Hässig, M., Rolland, Y., Sosson, M., Galoyan, G., Müller, C., Avagyan, A., Sahakyan, L., 2013.
833 New structural and petrological data on the Amasia ophiolites (NW Sevan-Akera suture
834 zone, Lesser Caucasus): Insights for a large-scale obduction in Armenia and NE Turkey.
835 Tectonophysics 588:135-153.
836
837 Hässig, M., Rolland, Y., Sahakyan, L., Sosson, M., Galoyan, Gh., Avagyan, A., Bosch, D., Müller,
838 C., 2015. Multi-stage metamorphism in the South Armenian Block during the Late Jurassic
839 to Early Cretaceous: Tectonics over south-dipping subduction of Northern branch of
840 Neotethys. Journal of Asian Earth Sciences 102:4-23.
841
842 Hesselbo, S.P., 1986. Pseudoleucite from the Gardar of South Greenland. Bulletin of
843 Geological Society of Denmark 35:11-17.
844
845 Horton, B.K., 2008. Detrital zircon provenance of Neoproterozoic to Cenozoic deposits in
846 Iran: Implications for chronostratigraphy and collisional tectonics. Tectonophysics
847 451:97-122.
848
849 Hou, Z., Tian, S., Yuan, Z., Xie, Y., Yin, S., Yi, L., Yang, Z., 2006. The Himalayan collision zone
850 carbonatites in western Sichuan, SW China: Petrogenesis, mantle source and tectonic
851 implication. Earth and Planetary Science Letters 244:234-250.
852
853 Innocenti, F., Mazzuoli, R., Pasquare, G., Radicati di Brozolo, F., Villari, F., 1982. Tertiary

854 and Quaternary volcanism of the Erzurum-Kars area (Eastern Turkey): geochronological
855 data and geodynamic evolution. Journal of Volcanology and Geothermal Research 13:223-
856 240.
857
858 Irvine, T.N., Baragar, W.R.A., 1971. A Guide to the Chemical Classification of the Common
859 Volcanic Rocks. Canadian Journal of Earth Sciences 8:523-548.
860
861 Jackson, J., Haines, J., Holt, W., 1995. The accommodation of Arabia–Eurasia Plate
862 convergence in Iran. Journal of Geophysical Research 100 (B8):15205-15219.
863
864 Jahn, B.-M., Wu, F., Lo, C.-H., Tsai, C.-H., 1999. Crust-mantle interaction induced by deep
865 subduction of the continental crust: geochemical and Sr-Nd isotopic evidence from post-
866 collisional mafi-ultramafic intrusions of the northern Dabie complex, central China.
867 Chemical Geology 157:119-146.
868
869 Johnson, S.E., Paterson, S.R., Tate, M.C., 1999. Structure and emplacement history of a
870 multiple-center, cone-sheet bearing ring complex: The Zarza Intrusive Complex, Baja
871 California, Mexico. Geological Society of America Bulletin 111:607-619.
872
873 Jrbashyan, R., 1990. Paleogene volcanic belts of closure zone of the Tethys Ocean. Thesis
874 of Doc. Sci. dissertation, Academy of Science, Georgian SSR, Tbilisi, Georgia (in Russian).
875
876 Jung, S., Mezger, K., Hoernes, S., 2004. The role of crustal contamination and source
877 composition in the petrogenesis of shear zone-related syenites (Damara belt, Namibia) —
878 constraints from U–Pb geochronology and Nd–Sr–Pb–O isotope compositions.

879 Contributions to Mineralogy and Petrology 148:104–121.
880
881 Jung, S., Hoernes, S., Hoffer, E., 2005. Petrogenesis of cogenetic nepheline and quartz
882 syenites and granites (northern Damara orogen, Namibia) — enriched mantle vs. crustal
883 contamination. Journal of Geology 113:651–672.
884
885 Kaislaniemi, L., van Hunen, J., Allen, M.B., Neill, I., 2014. Sublithospheric small-scale
886 convection — a mechanism for collision zone magmatism. Geology 42: 291–294.
887
888 Karakhanian, A., Jrbashian, R., Trifonov, V., Philip, H., Arakelian, S., Avagian, A., 2002.
889 Holocene-historical volcanism and active faults as natural risk factors for Armenia and
890 adjacent countries. Journal of Volcanology and Geothermal Research 113:319–344.
891
892 Karapetian, S., Jrbashian, R., Mnatsakanian, A., 2001. Late collision rhyolitic volcanism in
893 the north-eastern part of the Armenian highland. Journal of Volcanology and Geothermal
894 Research 112:189–220.
895
896 Kazemi, K., Kananian, A., Xia, Y., Sarjoughian, F., 2018. Petrogenesis of Middle-Eocene
897 granitoids and their Mafic microgranular enclaves in central Urmia-Dokhtar Magmatic
898 Arc (Iran): Evidence for interaction between felsic and mafic magmas. Geoscience
899 Frontiers, doi:10.1016/j.gsf.2018.04.006.
900
901 Kepezhinskas, P., McDermott, F., Defant, M.J., Hochstaedter, A., Drummond, M.S.,
902 Hawkesworth, C.J., Koloskov, A., Maury, R.C., Bellon, H., 1997. Trace element and Sr-Nd-

903 Pb isotopic constraints on a three-component model of Kamchatka arc petrogenesis.
904 Geochimica et Cosmochimica Acta 61:577-600.
905
906 Keskin, M., Pearce, J.A., Mitchell, J.G., 1998. Volcano-stratigraphy and geochemistry of
907 collision-related volcanism on the Erzurum-Kars Plateau, northeastern Turkey. Journal of
908 Volcanology and Geothermal Research 85:355–404.
909
910 Keskin, M., 2003. Magma generation by slab steepening and breakoff beneath a
911 subduction-accretion complex: an alternative model for collision-related volcanism
912 in Eastern Anatolia, Turkey. Geophysical Research Letters 30:1–4.
913
914 Kheirkhah, M., Allen, M.B., Emami, M., 2009. Quaternary syn-collision magmatism from
915 the Iran/Turkey borderlands. Journal of Volcanology and Geothermal Research 182:1-12.
916
917 Kheirkhah, M., Neill, I., Allen, M.B., 2015. Petrogenesis of OIB-like basaltic volcanic rocks
918 in a continental collision zone: Late Cenozoic magmatism of Eastern Iran. Journal of Asian
919 Earth Sciences 106:19-33.
920
921 Knipper, A.L., Khain, E.V., 1980. Structural position of ophiolites of the Caucasus. Ofioliti
922 2:297-314.
923
924 Kogarko, L.N., Konova, V.A., Orlova, M.P., Woolley, A.R.,1995. Caucasus (Armenia,
925 Azerbai'an, Georgia), in: Kogarko, L. (Ed.), Alkaline Rocks and Carbonatites of the
926 World,Part Two: Former USSR, Springer, Dordrecht, pp. 59-64.
927

928 Kotlyar, V.N., 1958. Pambak. Academy of Sciences, Armenian SSR, Yerevan (in Russian).
929
930 Kramm, U., Kogarko, L.N., 1994. Nd and Sr isotope signatures of the Khibina and Lovozero
931 agpaitic centres, Kola Province, Russia. Lithos 32:225-242.
932
933 La Flèche, M.R., Camiré, G., Jenner, G.A., 1998. Geochemistry of post-Acadian,
934 Carboniferous continental intraplate basalts from the Maritimes Basin, Magdalen Islands,
935 Québec, Canada. Chemical Geology 148:115-136.
936
937 Lan, T.-G., Fan, H.-R., Hu, F.-F., Tomkins, A.G., Yang, K.-F., Liu, Y., 2011. Multiple crust-
938 mantle interactions for the destruction of the North China Craton: Geochemical and Sr-
939 Nd-Pb-Hf isotopic evidence from the Longbaoshan alkaline complex. Lithos 122:87-106.
940
941 Laporte, D., Lambart, S., Schiano, P., Ottolini, L., 2014. Experimental derivation of
942 nepheline syenite and phonolite liquids by partial melting of upper mantle peridotites.
943 Earth and Planetary Science Letters 404:319-331.
944
945 Lebedev, V.A., Bubnov, S.N., Chernyshev, I.V., Chugaev, A.V., Dudauri, O.Z., Vashakidze, G.T.,
946 2007. Geochronology and genesis of subalkaline basaltic lava rivers at the Dzhavakheti
947 Highland, Lesser Caucasus: K-Ar and Sr-Nd isotopic data. Geochemistry International 45:
948 211-225.
949
950 Lebedev, V.A., Chernyshev, I.V., Shatagin, K.N., Bubnov, S.N., Yakushev, A.I., 2013. The
951 Quaternary Volcanic Rocks of the Geghama Highland, Lesser Caucasus, Armenia:
952 Geochronology, isotopic Sr-Nd characteristics, and origin. Journal of Volcanology and

953 Seismology 7:204-229.
954
955 Lebedev, V.A., Sakhno, V.G., Yakushev, A.I., 2009. Late Cenozoic volcanic activity in
956 Western Georgia: Evidence from new isotope geochronological data. Doklady Earth
957 Sciences 427:819-825.
958
959 Lordkipanidze, M.B., Meliksetian, B.M., Jrbashyan, R., 1989. Mesozoic-Cenozoic magmatic
960 evolution of the Pontian-Crimean-Caucasian region, in: Rakuš, M., Dercourt, J., Nairn,
961 A.E.M. (Eds.), Evolution of the northern margin of Tethys, IGCP project 198. Mémoire
962 Société Géologique France, Paris, Nouvelle Série, 154:103–124.
963
964 Mamani, M., Wörner, G., Sempere, T., 2010. Geochemical variations in igneous rocks of the
965 central Andean orocline (13°S-18°S): Tracing crustal thickening and magma generation
966 through time and space. Geological Society of America Bulletin 122:162-182.
967
968 Marks, M.A.W., Vennemann, T., Siebel, W., Markl, G., 2004. Nd-, O-, H-isotopic evidence for
969 complex, closed-system fluid evolution of the peralkaline Ilímaussaq intrusion, South
970 Greenland. Geochimica et Cosmochimica Acta 68:3379-3395.
971
972 Marks, M.A.W., Schilling, J., Coulson, I.M., Wenzel, T., Markl, G., 2008. The Alkaline–
973 Peralkaline Tamazeght Complex, High Atlas Mountains, Morocco: Mineral Chemistry and
974 Petrological Constraints for Derivation from a Compositionally Heterogeneous Mantle
975 Source. Journal of Petrology 49:1097-1131.
976

977 Mazhari, S.A., Bea, F., Amini, S., Ghalamghash, J., Molina, J.F., Montero, P., Scarrow, J.H.,
978 Williams, I.S., 2009. The Eocene bimodal Piranshahr massif of the Sanandaj-Sirjan Zone,
979 NW Iran: a marker of the end of the collision in the Zagros orogeny. Journal of the
980 Geological Society of London 166:53-69.
981
982 Mederer, J., Moritz, R., Ulianov, A., Chiaradia, M., 2013. Middle Jurassic to Cenozoic
983 evolution of arc magmatism during Neotethys subduction and arc-continent collision in
984 the Kapan Zone, southern Armenia. Lithos 177:61-78.
985
986 Meliksetian, B.M., 1970. About the problem of genesis of pseudoleucite and leucite bearing
987 rocks of Tezhsar Alkaline Complex. Earth Science Letters, Academy of Sciences, Armenian
988 SSR, Yerevan, vol. 3, pp. 61-85 (in Russian).
989
990 Meliksetian, B.M., 1971. Mineralogy, geochemistry and petrology of Tezhsar Alkaline
991 Complex, in: Intrusive complexes of principal ore provinces of Armenia. Academy of
992 Sciences, Armenian SSR, Yerevan, pp. 117-298 (in Russian).
993
994 Meliksetian, B.M., 1978. Genesis of Pambak pseudoleucites (Armenia), XI General Meeting
995 of International Mineralogical Association, Novosibirsk, Abstracts 1:36-37.
996
997 Meliksetian, B.M., 1989. Petrology, geochemistry and ore genesis of Palaeogene-Neogene
998 volcano-intrusive formations of Lesser Caucasus (magmatism of collision zones). Thesis
999 of Doc. Sci. dissertation, Academy of Science, Tbilisi, Georgian SSR (in Russian).
1000
1001 Melkonyan, R.L., Ghkasian, R.Kh., Tayan, R.N., Haruntunyan, M.A., 2008. Geochronometry

of the Meghri pluton monzonites (Armenia) – results and consequences. Proceedings of the National Academy of Sciences of the Republic of Armenia 61:3-9 (in Russian with English abstract).

Moritz, R., Rezeau, H., Ovtcharova, M., Tayan, R., Melkonyan, R., Hovakimyan, S., Ramazanov, V., Selby, D., Ulianov, A., Chiaradia, M., Putlitz, B., 2016. Long-lived, stationary magmatism and pulsed porphyry systems during Tethyan subduction to post-collision evolution in the southernmost Lesser Caucasus, Armenia and Nakhitchevan. Gondwana Research 37:465-503.

Neill, I., Meliksetian, Kh., Allen, M.B., Navarsardyan, G., Karapetyan, S., 2013. Pliocene-Quaternary volcanic rocks of NW Armenia: Magmatism and lithospheric dynamics within an active orogenic plateau. Lithos 180-181:200-215.

Neill, I., Meliksetian, Kh., Allen, M.B., Navasardyan, G., Kuiper, K., 2015. Petrogenesis of mafic collision zone magmatism: The Armenian sector of the Turkish-Iranian Plateau. Chemical Geology 403:24-41.

Nielsen T. F. D., 1987 Tertiary alkaline magmatism in East Greenland: a review, in: Fitton, J.G., Upton, B.G.J. (Eds.), Alkaline Igneous Rocks. Geological Society Special Publications 30:489-515.

Pearce, J.A., Bender, J.F., Delong, S.E., Kidd, W.S.F., Low, P.J., Guner, Y., Sargolu, F., Yilmaz, Y., Moorbath, S., Mitchell, J.G., 1990. Genesis of collision volcanism in eastern Anatolia, Turkey. Journal of Volcanology and Geothermal Research 44:189–229.

Phillip, H., A. Cicternas, A. Gvishiani, A. Gorshkuv, 1989. The Caucasus: an actual example of the initial stages of continental collision. Tectonophysics 161:1–21.

Pivec, E., Ulrych, J., Langrová, A., 2004. On the origin of pseudoleucite from Cenozoic phonolite dyke from Loučná/Böhmisch Wiesenthal, Krušné hory/Erzgebirge Mts., Bohemia. Neues Jahrbuch für Mineralogie – Abhandlungen 179:221-238.

Rezeau, H., Moritz, R., Leuthold, J., Hovakimyan, S., Tayan, R. & Chiaradia, M., 2017. 30 Myr of Cenozoic magmatism along the Tethyan margin during Arabia-Eurasia accretionary orogenesis (Meghri-Ordubad pluton, southernmost Lesser Caucasus). Lithos 288-289:108-124.

Riley, T.R., Bailey, D.K., Harmer, R.E., Liebsch, H., Lloyd, F.E., Palmer, M.R., 1999. Isotopic and geochemical investigation of a carbonatite-syenite-phonolite diatreme, West Eifel (Germany). Mineralogical Magazine 63:615-615.

Rock, N.M.S., 1976. Fenitisation around the Monchique alkaline complex, Portugal. Lithos 9:263-279.

Rolland, Y., 2017. Caucasus collisional history: Review of data from East Anatolia to West Iran. Gondwana Research 49:130-146.

Rolland, Y., Billo, S., Corsini, M., Sosson, M., Galoyan G., 2009a. Blueschists of the Amassia-Stepanavan Suture Zone (Armenia): linking Tethys subduction history from E-Turkey to

W-Iran. International Journal of Earth Sciences 98:533-550.

Rolland, Y., Galoyan, G., Bosch, D., Sosson, M., Corsini, M., Fornari, M., Verati, C., 2009b. Jurassic back-arc and Cretaceous hot-spot series in the Armenian ophiolites - Implications for the obduction process. Lithos 112:163-187.

Rosenbaum, G., Lister, G.S., Duboz, C., 2002. Relative motions of Africa, Iberia and Europe during Alpine orogeny. Tectonophysics 359:117-129.

Sahakyan, L., Bosch, D., Sosson, M., Avagyan, A., Galoyan, Gh., Rolland, Y., Bruguier, O., Stepanyan, Zh., Galland, B., Vardanyan, S., 2016. Geochemistry of the Eocene magmatic rocks from the Lesser Caucasus area (Armenia): evidence of a subduction geodynamic environment. Geological Society of London Special Publications 428:73.

Schiano, P., Monzier, M., Eissen, J.-P., Martin, H., Koga, K.T., 2010. Simple mixing as the major control of the evolution of volcanic suites in the Ecuadorian Andes. Contributions to Mineralogy and Petrology 160:297-310.

Sheth, H., Meliksetian, Kh., Gevorgyan, H., Israyelyan, A., Navasardyan, G., 2015. Intracanyon basalt lavas of the Debed River (northern Armenia), part of a Pliocene-Pleistocene continental flood basalt province in the South Caucasus. Journal of Volcanology and Geothermal Research 295:1-15.

Shand, S. J., 1947. The Eruptive Rocks. Wiley (3rd Ed.), New York.

1077 Sindern, S., Kramm, U., 2000. Volume characteristics and element transfer of fenite
1078 aureoles: a case study from the Iivaara alkaline complex, Finland. Lithos 51:75-93.
1079
1080 Smith, I.E.M., White A.J.R., Chappell B.W., Eggleton R.A., 1988. Fractionation in a zoned
1081 monzonite pluton: Mount Dromedary, southeastern Australia. Geological Magazine
1082 125:273-284.
1083
1084 Sosson, M., Rolland, Y., Müller, C., Danelian, T., Melkonyan, R., Kekelia, S., Adamia, S.,
1085 Babazadeh, V., Kangarli, T., Avagyan, A., Galoyan, G., Mosar, J., 2010. Subductions,
1086 obduction and collision in the Lesser Caucasus (Armenia, Azerbaijan, Georgia), new
1087 insights. Geological Society Special Publications 340:329-352.
1088
1089 Suikkanen, E., Rämö, O.T., 2017. Metasomatic alkali-feldspar syenites (episyenites) of the
1090 Proterozoic Suomenniemi rapakivi granite complex, southeastern Finland. Lithos 294-
1091 295:1-19.
1092
1093 Taylor, D., MacKenzie, W.S., 1975. A contribution to the pseudoleucite problem.
1094 Contributions to Mineralogy and Petrology 49:321-333.
1095
1096 Tempelman-Kluit, D.J., 1969. A re-examination of pseudoleucite from Spotted Fawn Creek,
1097 west-central Yukon. Canadian Journal of Earth Sciences 6:55-62.
1098
1099 Trumbull, R.B., Bühn, B., Romer, R.L. & Volker, F., 2003. The petrology of basanite-tephrite
1100 intrusions in the Erongo Complex and implications for a plume origin of Cretaceous
1101 alkaline complexes in Namibia. Journal of Petrology 44:93-112.

Upton, B.G.J., Emeleus, C.H., Heaman, L.M., Goodenough, K.M., Finch, A.A., 2003. Magmatism of the mid-Proterozoic Gardar Province, South Greenland: chronology, petrogenesis and geological setting. Lithos 68:43-65.

Uto, K., Ishizuka O., Matsumoto A., Kamioka H., Togashi S., 1997 Laser-heating $^{40}Ar/^{39}Ar$ dating system of the Geological Survey of Japan: system outline and preliminary results. Bulletin of Geological Survey of Japan 48:23–46.

Van Hunen, J., Allen, M.B., 2011. Continental collision and slab break-off: A comparison of 3-D numerical models with observations. Earth and Planetary Science Letters 302:27-37.

Verdel, C.S., Wernicke, B.P., Ramezani, J., Hassanzadeh, J., Renne, P.R., Spell, T.L., 2007. Geology and thermochronology of Tertiary Cordilleran-style metamorphic core complexes in the Saghand region of central Iran. Geological Society of America Bulletin, 119:961–977.

Verdel, C., Wernicke, B.P., Hassanzadeh, J., Guest, B., 2011. A Paleogene extensional arc flare-up in Iran. Tectonics 30, TC3008, doi:10.1029/2010TC002809.

Viladkar, S.G., 2010. The origin of pseudoleucite in tinguaite, Ghori, India: a re-evaluation. Petrology 18:544-554.

Vincent, S.J., Morton, A.C., Carter, A., Gibbs, S., Barabadze, T.G., 2007. Oligocene uplift of the Western Greater Caucasus: an effect of initial Arabia-Eurasia collision. Terra Nova

19:160-166.

Williams, H.M., Turner, S.P., Pearce, J.A., Kelley, S.P., Harris, N.B.W., 2004. Nature of the source regions for post-collisional potassic magmatism in southern and northern Tibet from geochemical variations and inverse trace element modelling. Journal of Petrology 45:555–607.

Woodhead, J.D., Hergt, J.M., Davidson, J.P., Eggins, S.M., 2001. Hafnium isotope evidence for 'conservative' element mobility during subduction zone processes. Earth and Planetary Science Letters 192:331-346.

Woolley A. R. & Jones G. C., 1987 The petrochemistry of the northern part of the Chilwa alkaline province, Malawi, in: Fitton, J.G., Upton, B.G.J. (Eds.), Alkaline Igneous Rocks, Geological Society Special Publications 30:335-355.

Woolley, A.R., 2001. Alkaline Rocks and Carbonatites of the World, Part 3: Africa. The Geological Society, London.

Yagi, K., Gupta, A.K., 1978. Pseudoleucite from Tezhsarsk, USSR, and its genesis. XI General Meeting of International Mineralogical Association, Novosibirsk, Abstracts 1, 38-39.

Zavaricky, A., 1934. About pseudoleucite and epileucite rocks. Reports of the Academy of Sciences SSSR, N8-9.

Zhang, K.-J., Li, Q.-H., Yan, L.-L., Zeng, L., Lu, L., Zhang, Y.-X., Hui, J., Jin, X, Tang, X.-C., 2017.

Geochemistry of limestones deposited in various plate tectonic settings. Earth-Science Reviews 167:27-64.

Zhao, Z.-F., Dai, L.-Q., Zheng, J.-F., 2013. Post-collisional mafic igneous rocks record crust-mantle interaction during continental deep subduction. Nature Scientific Reports 3:3413.

Zhou, X.M., Li, W.X., 2000. Origin of late Mesozoic igneous rocks in south eastern China: implications for lithosphere subduction and underplating of mafic magmas. Tectonophysics 326:269-287.

Figure captions

Figure 1 – (a) Geotectonic framework of the Caucasus region showing major tectonostratigraphic provinces, associated terranes and the location of Tezhsar Alkaline Complex (star) about 50 km north of Yerevan (modified after Adamia et al., 2011, and Rezeau et al., 2017). (b) Palaeogeographical reconstruction of the Eurasian-Arabian collision in the Ypresian (52Ma) just before formation of TAC (modified after Mederer et al., 2013). SAB – South Armenian Block, SAS – Sevan-Akera Suture, BZS – Bitlis-Zagros Suture, TAB –Tauride-Anatolian Block, NTP – Northern Tethyan Province, STP – Southern Tethyan Province.

Figure 2 – Geological map of the Tezhsar Alkaline Complex. The inset show a simplified subdivision of the TAC which is used for the geochemical diagrams of this study.

Figure 3 – Field relations (a, b) and hand specimen photographs (c, d) of the TAC. (a) Light coloured syenite intruding into dark grey volcanic rocks of the Outer Volcanic Unit. (b) Coarse-grained nepheline syenite pegmatite comprising dark patches of garnet and amphibole. (c) Phonolite handspecimen with idiomorphic leucite pseudomorphs reaching up to 2 cm in diameter. (d) Polished surface of a pseudoleucite phonolite. (e, f) Hand specimen of pseudoleucite megacrysts (up to ~8cm in diameter) as deltoidal icositetrahedra found in TAC phonolites. Samples are from old collections of B. Meliksetian and Z. Chibukhcyan.

Figure 4 – Photomicrographs illustrating characteristic features of rocks from the TAC in plane polarized (PPL) and cross-polarized (XPL) light. (a) Plagioclase (Pl) phenocrysts in

feldspathic matrix of a basaltic trachyandesite, OVU (XPL). (b) Biotite (Bt) surrounded by clinopyroxene (Cpx) with accessory apatite (Ap) in trachyte, CVU (PPL). (c) Clinopyroxene and titanite (Ttn) in nepheline syenite, SYU (PPL). (d) Amphibole (Amp) in syenite, SYU (PPL). (e) Sodalite (Sdl) and nepheline (Nph) in nepheline syenite, SYU (PPL). (f) Amphibolitization of clinopyroxene in syenite, SYU (PPL) (g) Garnet (Grt) in syenite with inclusions of alkali feldspar, SYU (PPL) (h) Garnet-amphibole cluster with alkali feldspar and nepheline in pegmatitic nepheline syenite, SYU (PPL).

Figure 5 – (a) Total Alkali-Silica (TAS) classification diagram of the volcanic units (OVU and CVU) of the TAC. Alkaline-subalkaline division from Irvine & Baragar (1971). (b) R1-R2 classification diagram (from De La Roche et al., 1980) of the intrusive SYU unit of the TAC. (c) A/NK vs A/CNK diagram (after Shand, 1947) based on the molecular proportions of Al (A), Na (N), K (K) and Ca (C), showing that the rocks of the TAC can largely be classified as metaluminous. (d) Modified Alkali-Lime Index (MALI, after Frost and Frost, 2008) plotted as a function of SiO_2 content for the TAC rocks that are generally alkalic in composition. Comparative data for Eocene magmatic rocks from the Talysh mountains, Azerbaijan (Vincent et al., 2005 – pink diamonds) and Pliocene-Quaternary volcanic rocks from central and northern Armenia (Neill et al., 2013, 2015 – orange field).

Figure 6 – Harker diagrams of the TAC samples for selected major (a-c) and trace (d-f) elements. The limestone assimilation trend in (c) was calculated after Costa et al. (2013) using limestone composition WGZ-3 from Zhang et al. (2017). All symbols as in Fig. 5.

Figure 7 – (a) Chondrite-normalised REE diagram highlighting more pronounced LREE fractionation and negative Eu anomalies within the SYU relative to the volcanic units of

1211 the TAC. Normalisation values from Boynton et al. (1984). (b-d) Mantle-normalised trace
1212 element diagrams of rocks from the TAC; (b) – OVU, (c) – SYU, (d) – CVU. Normalisation
1213 values after McDonough & Sun, 1995. Comparative data from Neill et al. (2015) for
1214 Pliocene-Quaternary volcanic rocks from central and northern Armenia.
1215
1216 **Figure 8** – $^{40}Ar/^{39}Ar$ age spectrum plot for the amphibole separate from syenite sample
1217 6-8-12.
1218
1219 **Figure 9** – Sr-Nd isotope diagram of the TAC data (red squares) in comparison to other
1220 Eocene-Quaternary igneous rocks in the Lesser Caucasus and adjacent regions. The
1221 mantle array is from Lebedev et al. (2007) after DePaolo & Wasserburg (1979). Data
1222 sources: (I) – Moritz et al. (2017); (II) – Aydınçakçır & Şen, (2013); (III) – Kazemi et al.
1223 (2018); (IV) – Mazhari et al. (2009); (V) – Connor et al. (2011); (VI) – Kheirkhah et al.
1224 (2009); (VII) – Neill et al. (2013; 2015) . Literature data were recalculated using the ^{87}Rb
1225 decay constant of 1.3972×10^{-11} a^{-1}.
1226
1227 **Figure** 10 – TAC samples plotted in various diagrams to evaluate effects of distinct
1228 magmatic processes. (a) Rb/Nd vs. Rb diagram (after Schiano et al. 2010) where
1229 horizontal trends reflect fractional crystallization and positive correlations can be caused
1230 by mixing or batch partial melting. (b) Rb vs. Rb/V diagram (after Schiano et al. 2010)
1231 where curved trends, as observed for the TAC rocks, reflect fractional crystallisation or
1232 mixing. (c) Rb/Ba vs. Ba diagram exhibiting a smooth trend indicative of feldspar
1233 fractionation. (d) Initial $^{87}Sr/^{86}Sr$ isotope ratios of the TAC samples plotted against SiO_2
1234 content. All samples except one plot in a very narrow range of $(^{87}Sr/^{86}Sr)_i$ ratios and there
1235 is no clear trend with increasing SiO_2 content. The sample with the elevated $(^{87}Sr/^{86}Sr)_i$

ratio (2-7-09) has a high Rb/Sr ratio of ~8 and might be affected by post-magmatic Rb and/or Sr mobilization and a larger uncertainty in recalculation.

Figure 11 – Major and trace element indicators for fractionation and source enrichment processes. (a) CaO/Al_2O_3 vs FeO_t/MgO diagram showing fractionation trends for plagioclase, olivine and amphibole(am)/clinopyroxene(cpx) after Moritz et al. (2016). (b) Eu/Eu* vs SiO_2 diagram depicting negative Eu anomalies in SYU and CVU samples, indicating plagioclase fractionation. (c) Dy/Yb vs SiO_2 diagram with fractionation trends for garnet and amphibole after Davidson et al. (2007). (d) La/Sm vs Sm/Yb diagram with approximate mineral stability thresholds of in mantle melt residues after Mamani et al. (2010). Note the distinct signatures for the two volcanic units of TAC. (e) Ba vs Nb/Y diagram displaying trends for fluid enrichment due to slab dehydration and mantle-derived melt enrichments after Kepehinskas et al. (1997). Slab fluid enrichment is prominent in the OVU rocks. (f) Th/Yb vs Ba/La diagram with trends for enrichment from subducted slab sediments and slab fluids from Woodhead et al. (2001). Elevated Ba/La ratios in OVU rocks suggest source enrichment via slab fluids.

Figure 12 – Trace element ratio diagrams of TAC rocks. (a) Ba/Nb vs La/Nb. Alkali feldspar fractionation trend highlighted as a result of Ba depletion. Field boundaries after Jahn et al. (1999). (b) $(Ta/La)_N$ vs $(Hf/Sm)_N$. Influence of subduction metasomatism is suggested by strongly decreasing $(Ta/La)_N$ ratios. Field boundaries after La Flèche et al. (1998). Comparative data for Eocene magmatic rocks from the Talysh mountains, Azerbaijan (Vincent et al., 2005 – pink diamonds) and Pliocene-Quaternary volcanic rocks from central and northern Armenia (Neill et al., 2013, 2015 – orange field).

Figure 13 – Pseudoleucite from the OVU of the Tezhsar Complex. (a) Scanned thin section image of a single pseudoleucite crystal. (b,c) Back-scattered electron images of (b) the boundary between matrix and pseudoleucite and (c) the interior of the pseudoleucite. Note the presence of cancrinite (Ccn) and analcime (Anl), other mineral abbreviations as in Figure 4.

Figure 1

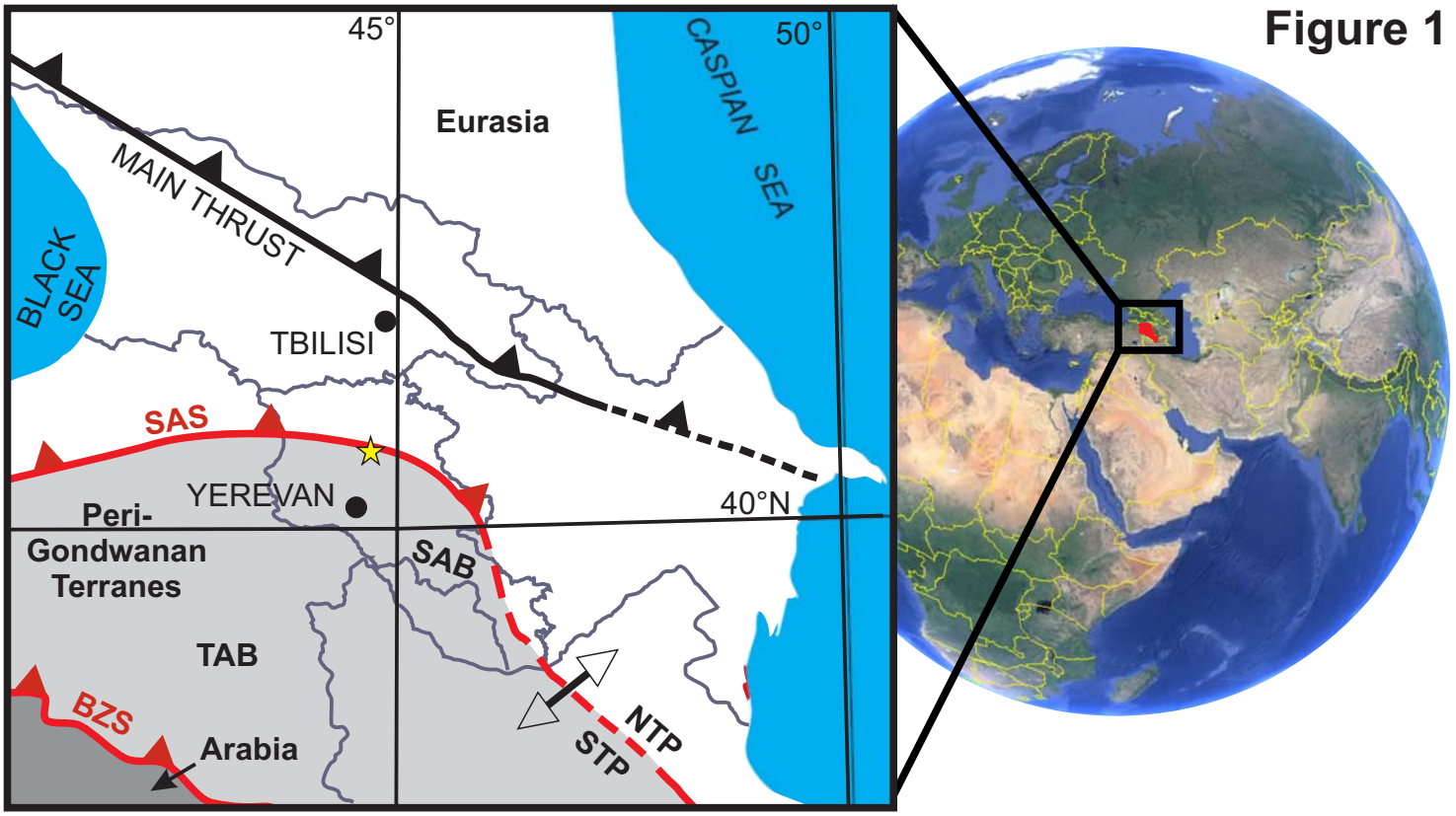
45°
50°
Eurasia
CASPIAN SEA
MAIN THRUST
BLACK SEA
TBILISI
SAS
YEREVAN
Peri-
Gondwanan
Terranes
40°N
SAB
TAB
BZS
Arabia
NTP
STP

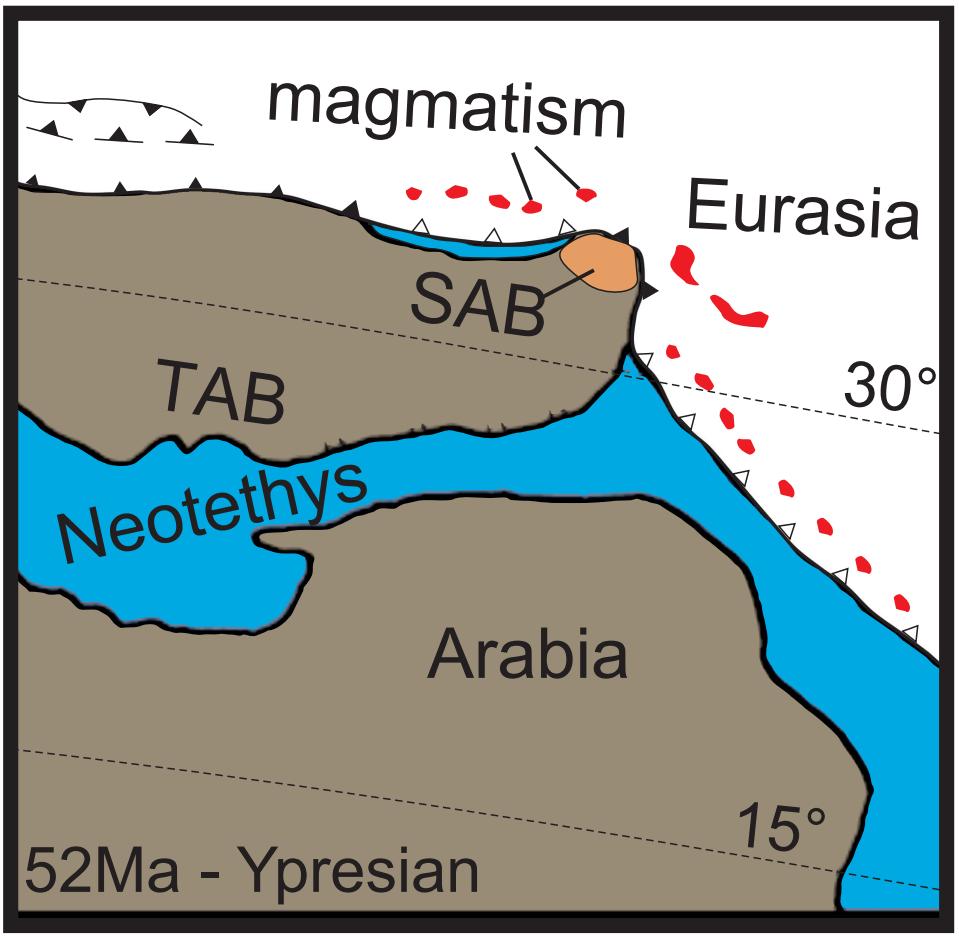
magmatism
Eurasia
SAB
TAB
30°
Neotethys
Arabia
15°
52Ma - Ypresian

Figure 2

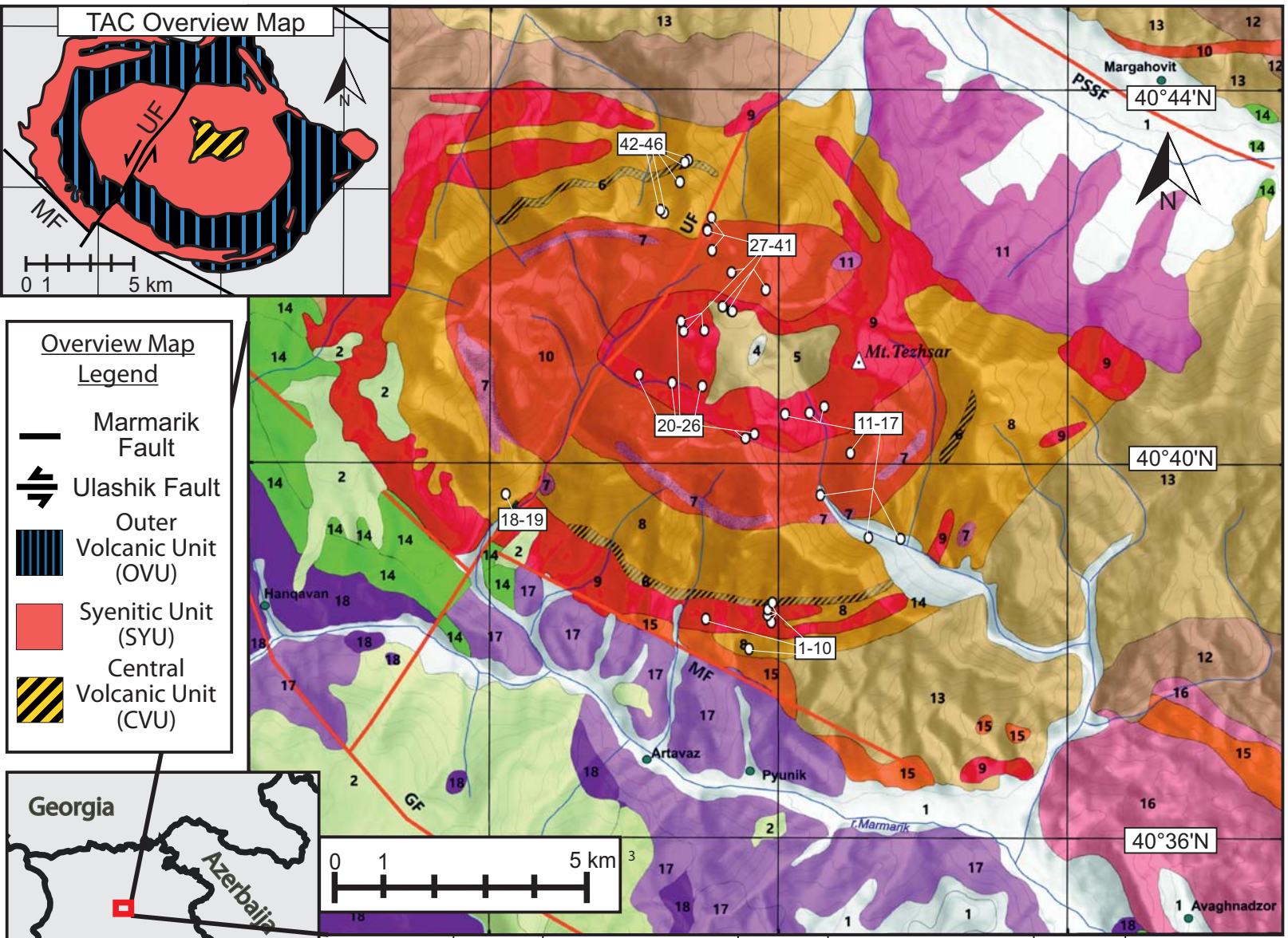

Legend

Holocene/ Recent	Alluvial Sediments	1
Late Miocene-Early Pliocene	Upper Suite: Andesites, dacites, trachydacites	2
	Lower Suite: Rhyolites, obsidians, tuffs, tuff breccias	3
Late Eocene: Tezhsar volcano-intrusive alkaline ring complex (comprises OVU, SYU & CVU generalised units)	Conduit: Trachytes, eruptive breccias with xenoliths of nepheline syenites and metamorphic basement	4
	Dykes and lavas of trachyandesites, trachytes and pseudoleucite trachyphonolites	5
	Ring dykes of pseudoleucite porphyric trachyphonolites-syenites	6
	Ring dykes, pseudoleucite syenites	7
	Trachyandesites, trachytes, pseudoleucite trachyphonolites-phonolites. Subvolcanic alkaline basalts, basanites, leucitites. Rare dykes of porphyric syenites, essexites & lamprophyres	8
	Syenites	9
	Nepheline syenites	10
Late Eocene	Porphyry granosyenites of Margahovit pluton	11
	Pambak Suite: Trachyandesites, basaltic-trachyandesites, alkali rhyolites	12
Middle Eocene	Basaltic, andesitic lavas, sub-volcanic bodies, breccias, tuffs	13
Upper Cretaceous	Sedimentary suite: Limestones, marls, clays, sandstones	14
Late Eocene	Porphyric quartz syenites Complex	15
	Aghavnadsor monzonite-syenite Complex	16
	Tonalite-granodiorite Complex	17
Middle-Late Proterozoic	Metamorphic Basement: Quartz-mica schists, quartz-mica-graphite schists. Quartz-chlorite-muscovite-biotite schists, amphibolites, gneisses.	18

Figure 3

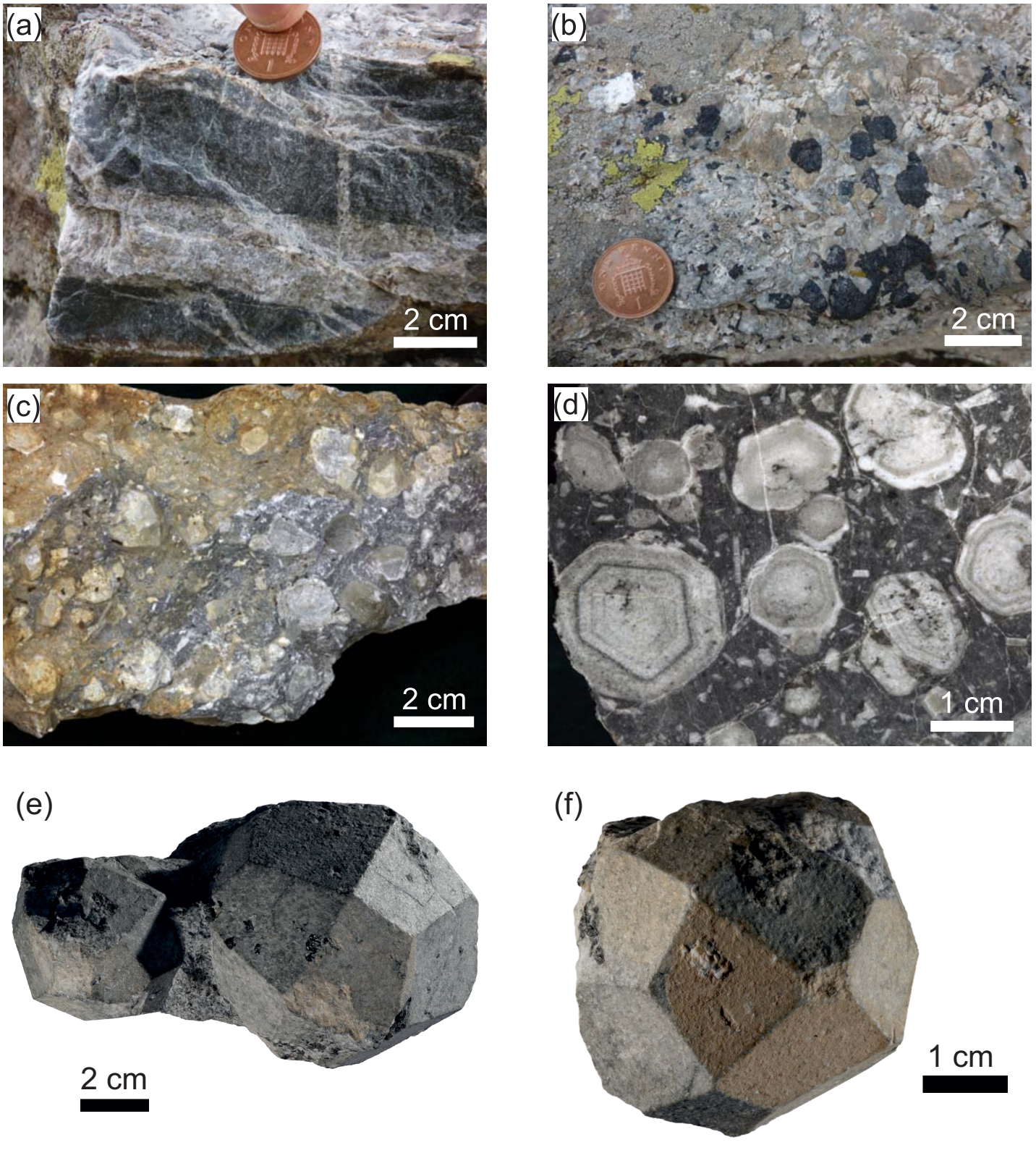

Figure 4

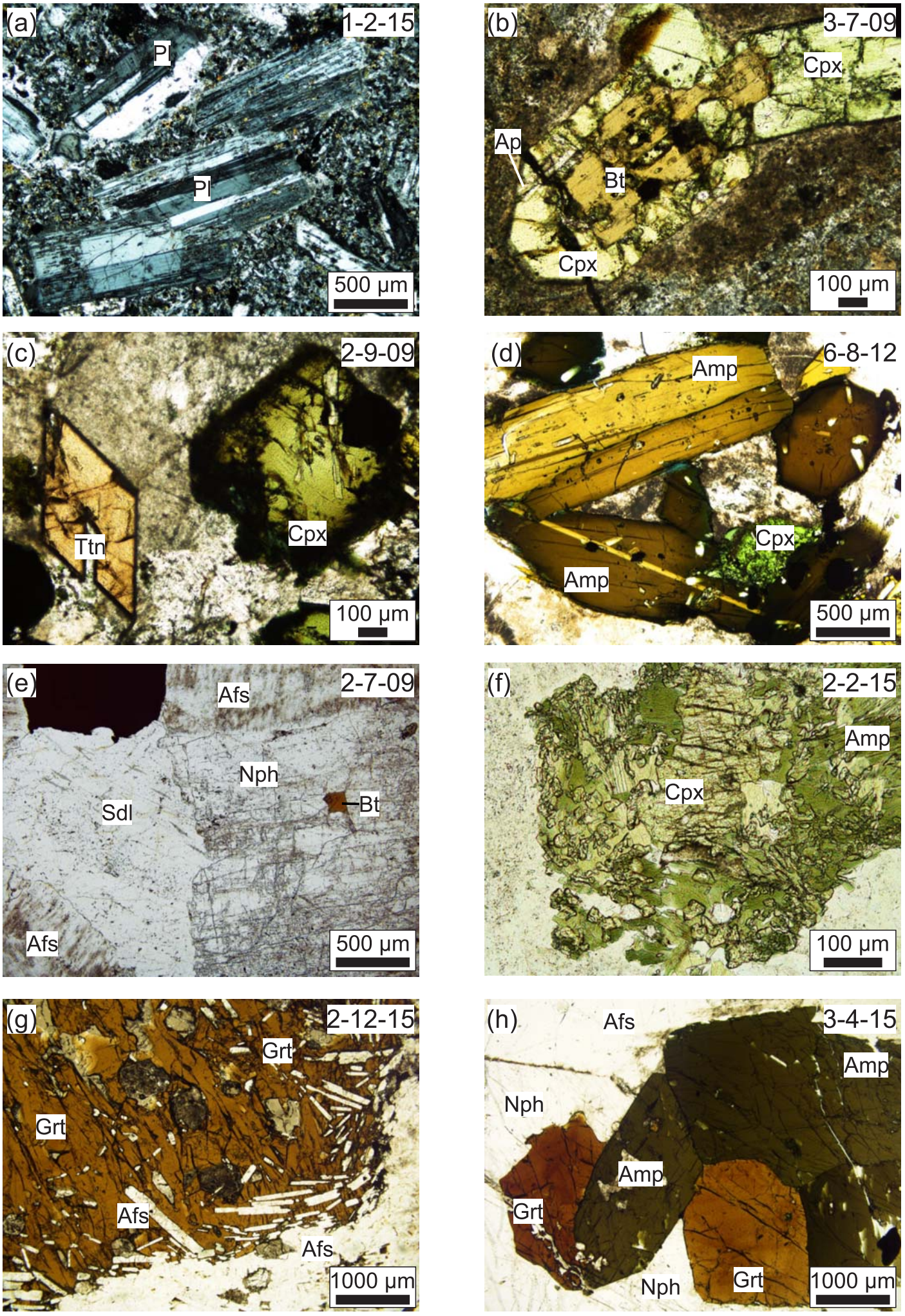
(a)
1-2-15
Pl
Pl
500 µm
(b)
3-7-09
Cpx
Ap
Bt
Cpx
100 µm
(c)
2-9-09
Ttn
Cpx
100 µm
(d)
6-8-12
Amp
Cpx
Amp
500 µm
(e)
2-7-09
Afs
Nph
Sdl
Bt
Afs
500 µm
(f)
2-2-15
Amp
Cpx
100 µm
(g)
2-12-15
Grt
Grt
Afs
Afs
1000 µm
(h)
Afs
3-4-15
Amp
Nph
Amp
Grt
Nph
Grt
1000 µm

Figure 5

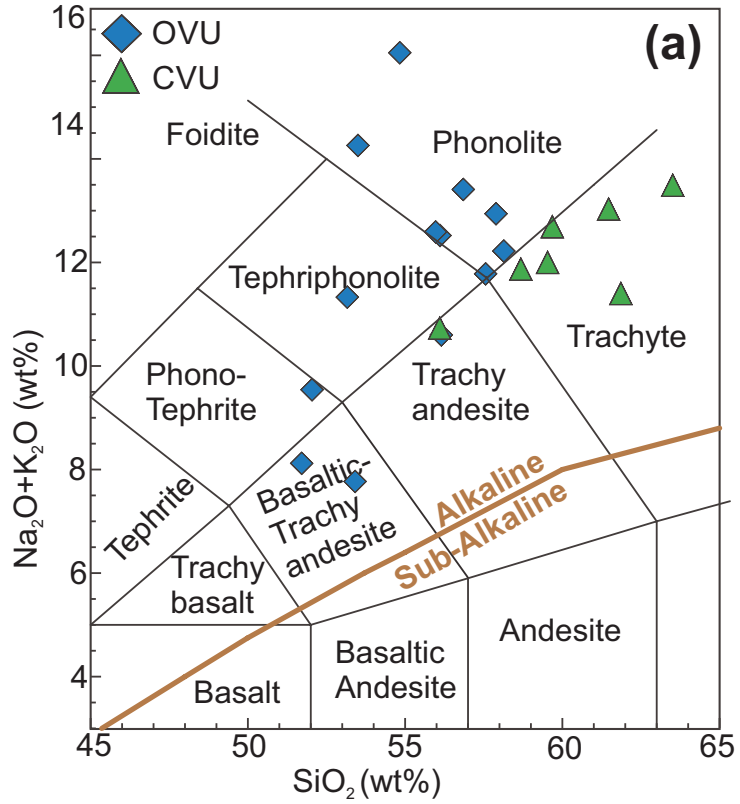
(a)
OVU
CVU
Foidite
Phonolite
Tephriphonolite
Trachyte
Phono-
Tephrite
Trachy
andesite
Tephrite
Basaltic-
Trachy
andesite
Alkaline
Sub-Alkaline
Trachy
basalt
Andesite
Basaltic
Andesite
Basalt
16
14
12
10
8
6
4
45
50
55
60
65
Na2O+K2O (wt%)
SiO2 (wt%)

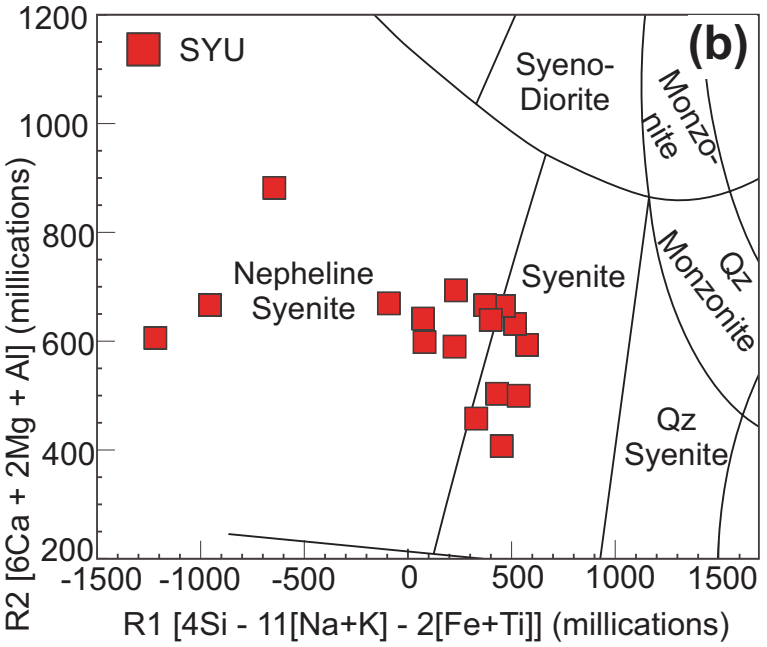
(b)
SYU
Syeno-
Diorite
Monzo-
nite
Qz
Monzonite
Nepheline
Syenite
Syenite
Qz
Syenite
1200
1000
800
600
400
200
-1500
-1000
-500
0
500
1000
1500
R2 [6Ca + 2Mg + Al] (millications)
R1 [4Si - 11[Na+K] - 2[Fe+Ti]] (millications)

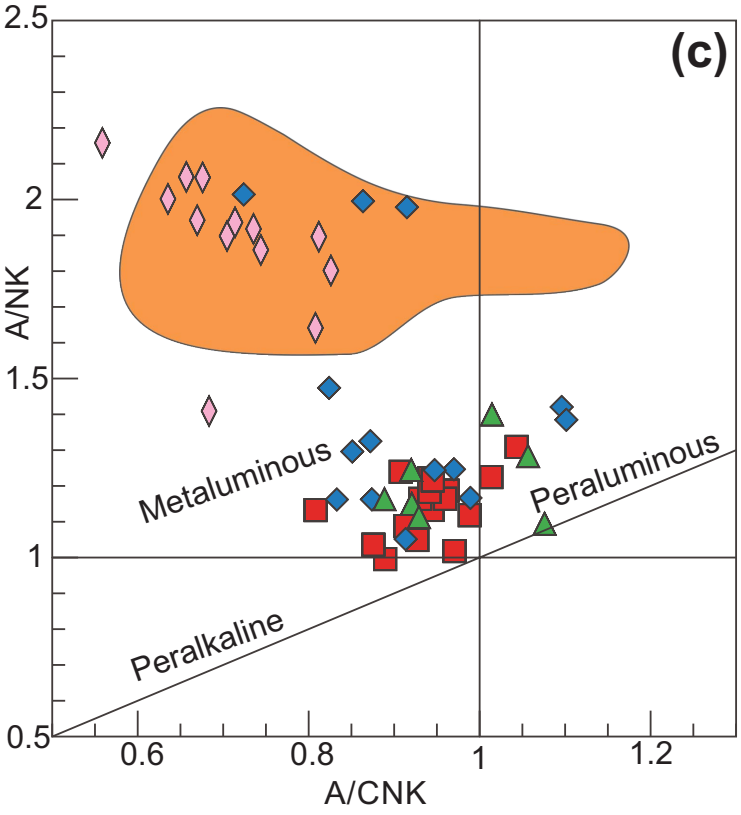
(c)
Metaluminous
Peraluminous
Peralkaline
2.5
2
1.5
1
0.5
0.6
0.8
1
1.2
A/NK
A/CNK

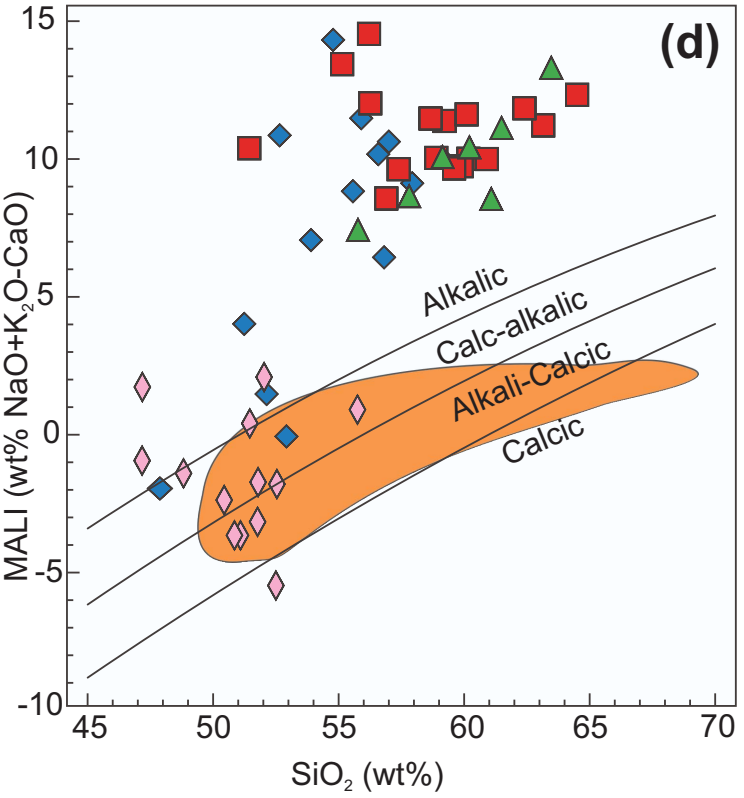
(d)
Alkalic
Calc-alkalic
Alkali-Calcic
Calcic
15
10
5
0
-5
-10
45
50
55
60
65
70
MALI (wt% NaO+K2O-CaO)
SiO2 (wt%)

Figure 6

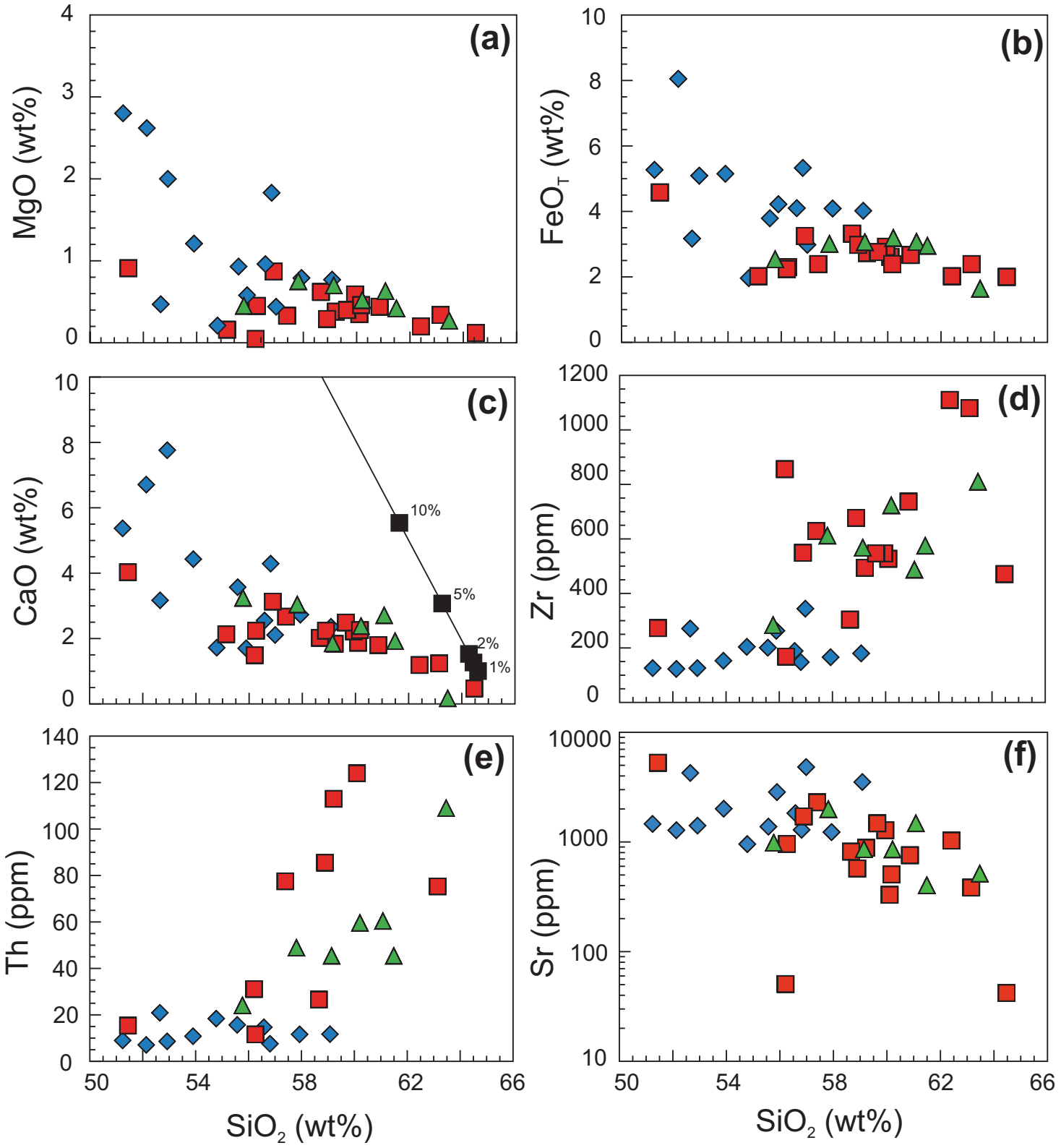
(a)
MgO (wt%)
(b)
FeO$_T$ (wt%)
(c)
CaO (wt%)
10%
5%
2%
1%
(d)
Zr (ppm)
(e)
Th (ppm)
(f)
Sr (ppm)
SiO$_2$ (wt%)
SiO$_2$ (wt%)

Figure 7

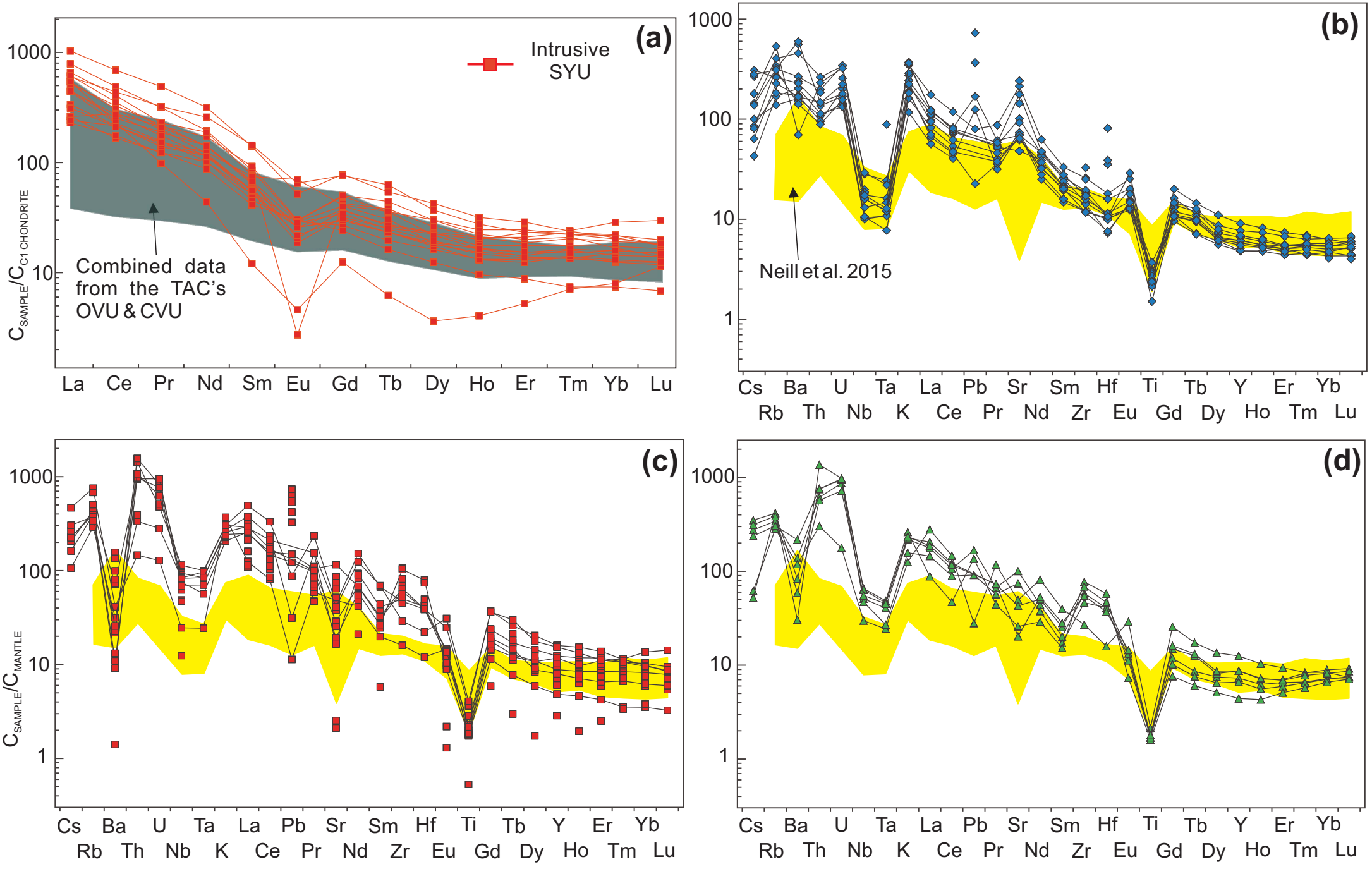
(a)
Intrusive SYU
Combined data from the TAC's OVU & CVU
$C_{SAMPLE}/C_{C1\ CHONDRITE}$
1000
100
10
La Ce Pr Nd Sm Eu Gd Tb Dy Ho Er Tm Yb Lu
(b)
Neill et al. 2015
1000
100
10
1
Cs Rb Ba Th U Nb Ta K La Ce Pb Pr Sr Nd Sm Zr Hf Eu Ti Gd Tb Dy Y Ho Er Tm Yb Lu
(c)
C_{SAMPLE}/C_{MANTLE}
1000
100
10
1
Cs Rb Ba Th U Nb Ta K La Ce Pb Pr Sr Nd Sm Zr Hf Eu Ti Gd Tb Dy Y Ho Er Tm Yb Lu
(d)
1000
100
10
1
Cs Rb Ba Th U Nb Ta K La Ce Pb Pr Sr Nd Sm Zr Hf Eu Ti Gd Tb Dy Y Ho Er Tm Yb Lu

Figure 8

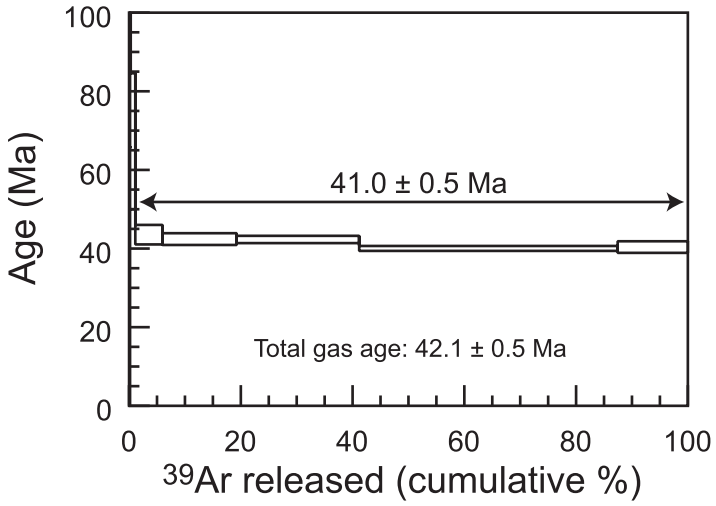
100
80
60
40
20
0
Age (Ma)
41.0 ± 0.5 Ma
Total gas age: 42.1 ± 0.5 Ma
0
20
40
60
80
100
39Ar released (cumulative %)

Figure 9

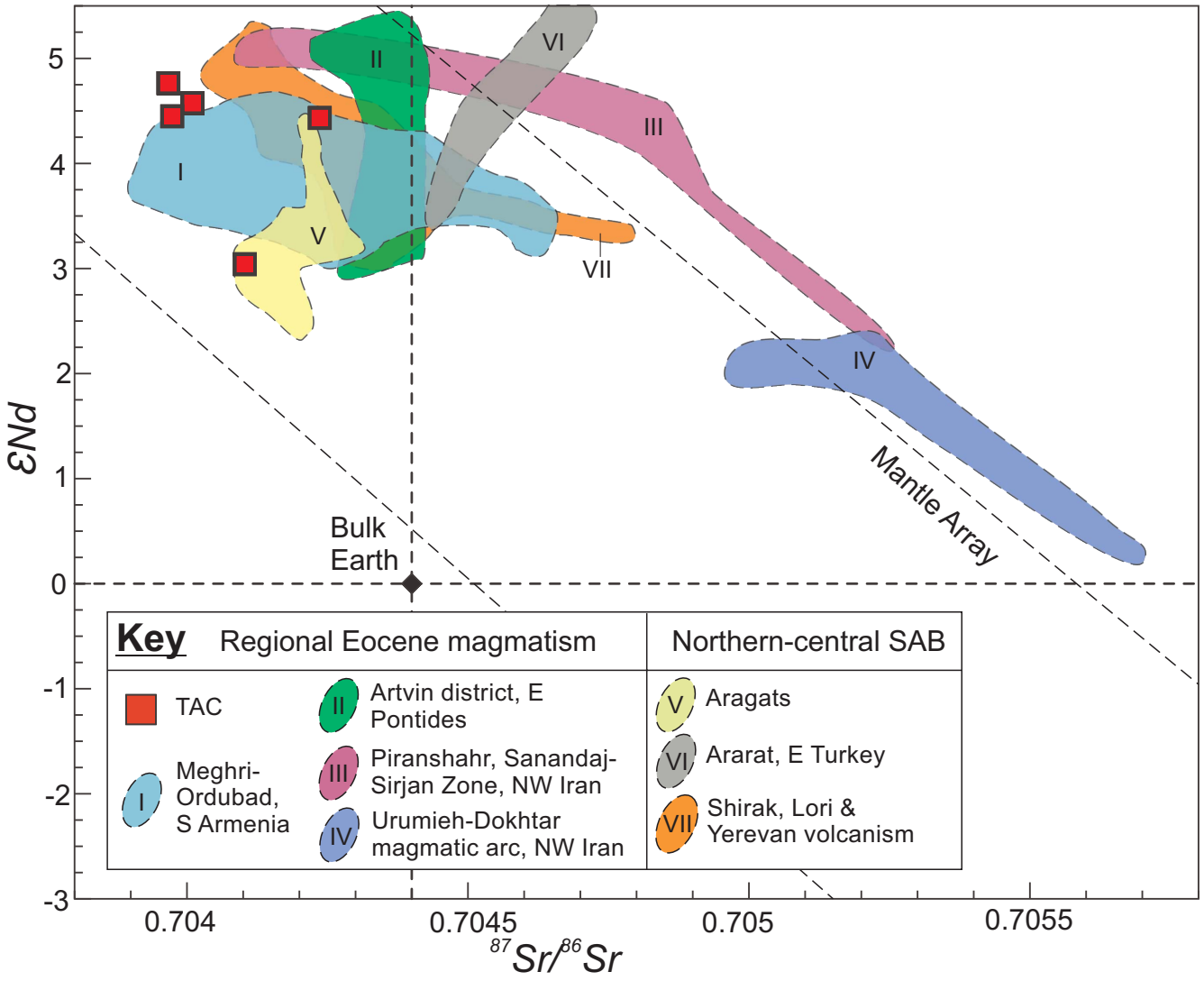
εNd
5
4
3
2
1
0
-1
-2
-3
0.704
0.7045
0.705
0.7055
87Sr/86Sr
I
II
III
IV
V
VI
VII
Bulk Earth
Mantle Array
Key
Regional Eocene magmatism
Northern-central SAB
TAC
Meghri-Ordubad, S Armenia
Artvin district, E Pontides
Piranshahr, Sanandaj-Sirjan Zone, NW Iran
Urumieh-Dokhtar magmatic arc, NW Iran
Aragats
Ararat, E Turkey
Shirak, Lori & Yerevan volcanism

Figure 10

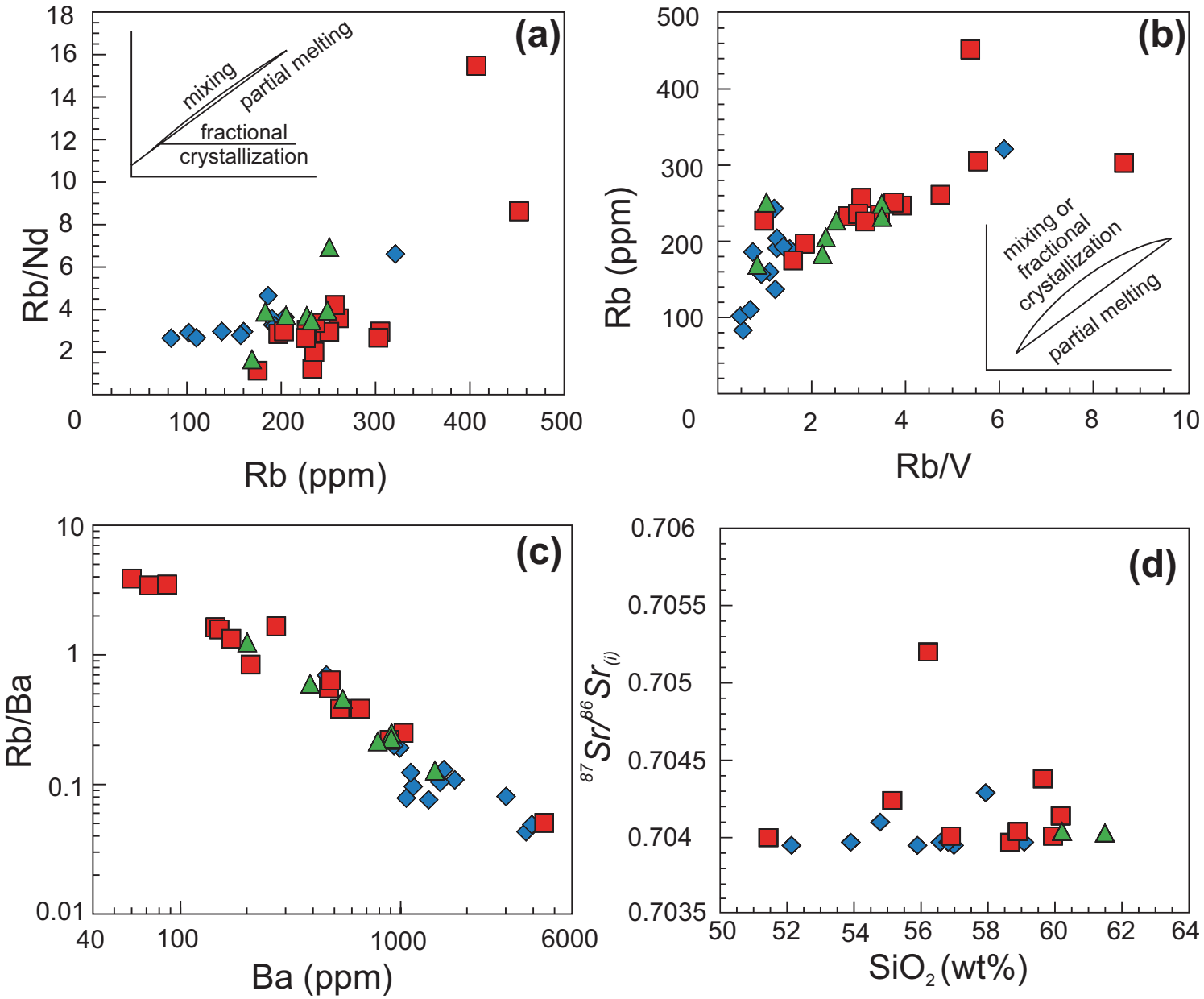
(a)
Rb/Nd
Rb (ppm)
mixing
partial melting
fractional
crystallization
(b)
Rb (ppm)
Rb/V
mixing or
fractional
crystallization
partial melting
(c)
Rb/Ba
Ba (ppm)
(d)
$^{87}Sr/^{86}Sr_{(i)}$
SiO_2 (wt%)

Figure 11

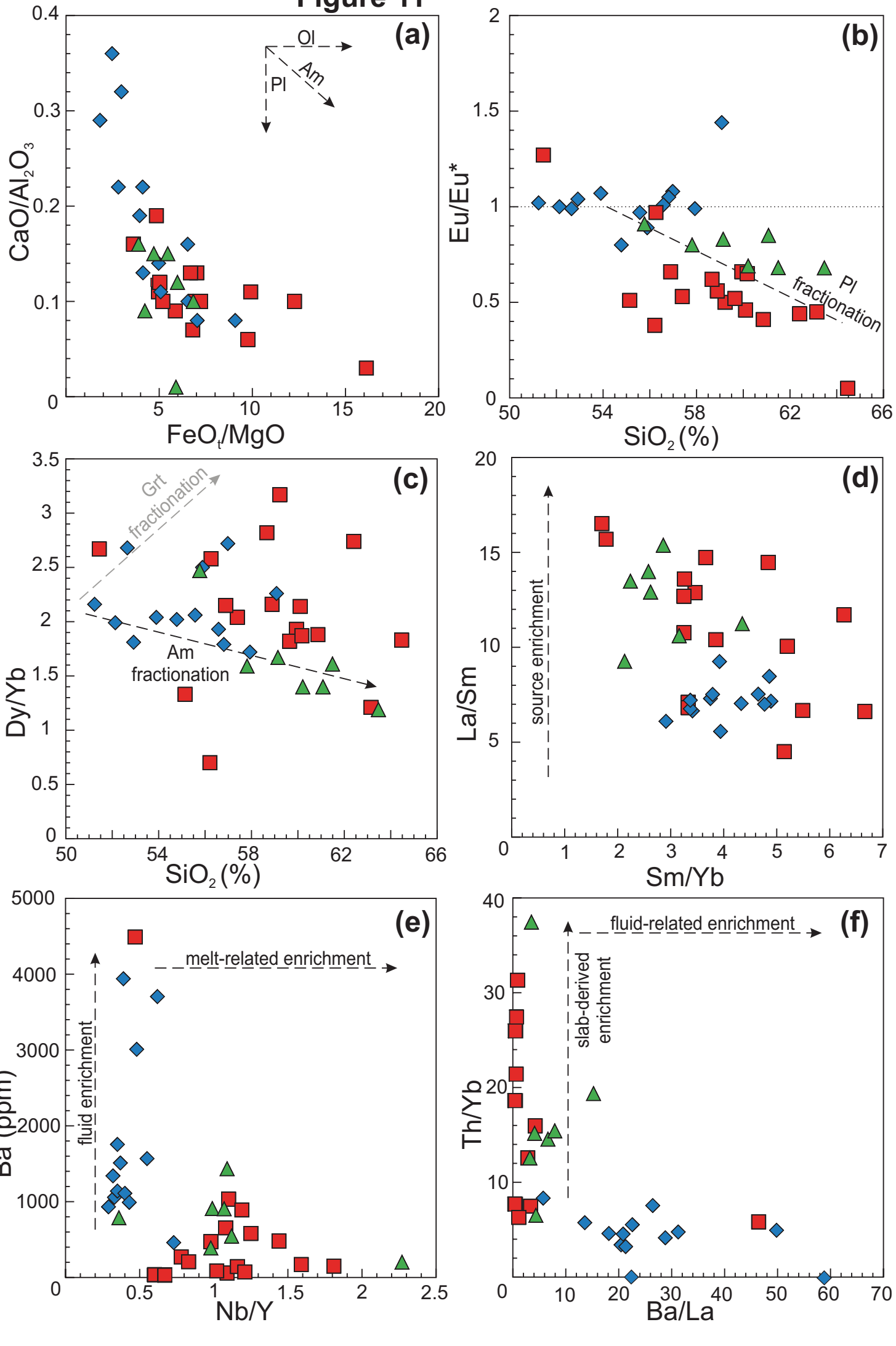
(a)
Ol
Am
Pl
CaO/Al2O3
FeOt/MgO
(b)
Eu/Eu*
Pl
fractionation
SiO2 (%)
(c)
Grt
fractionation
Am
fractionation
Dy/Yb
SiO2 (%)
(d)
source enrichment
La/Sm
Sm/Yb
(e)
melt-related enrichment
fluid enrichment
Ba (ppm)
Nb/Y
(f)
fluid-related enrichment
slab-derived
enrichment
Th/Yb
Ba/La

Figure 12

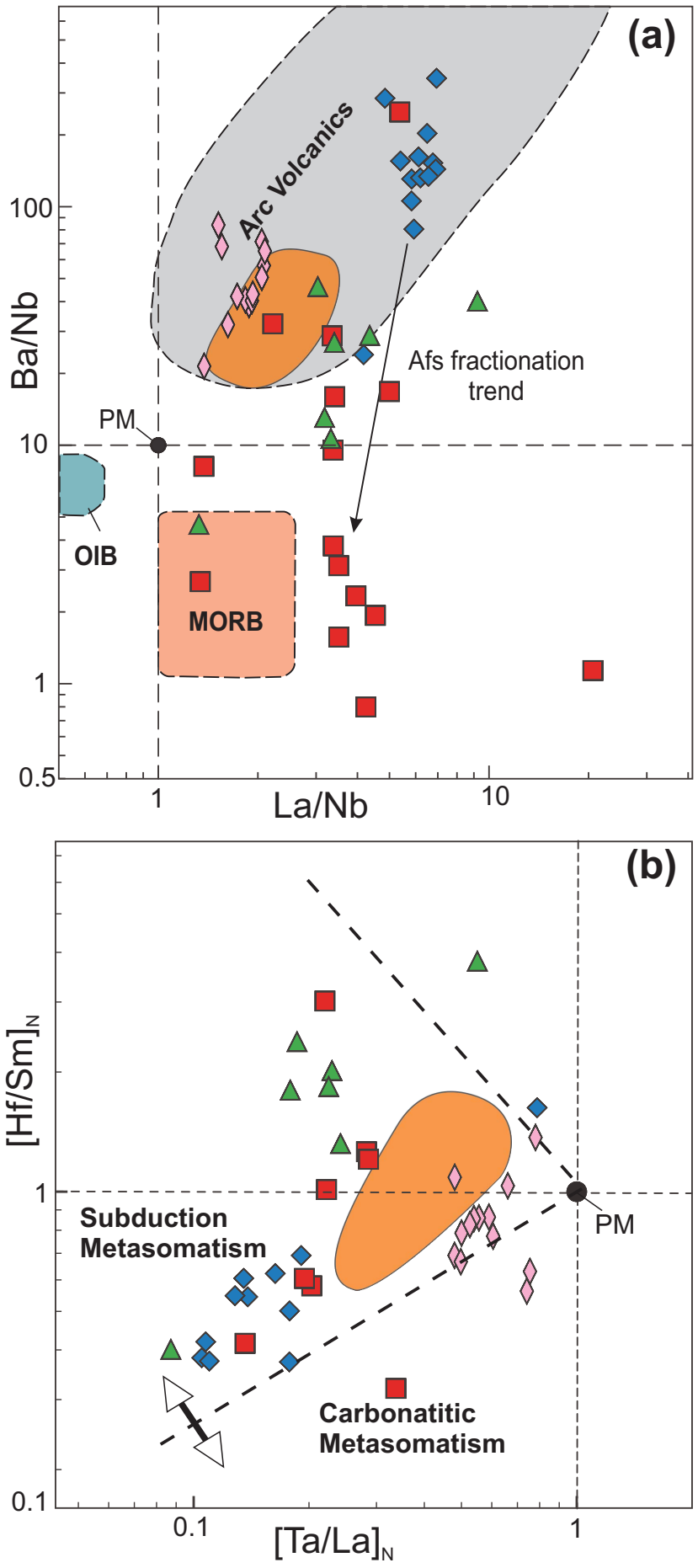
(a)
Arc Volcanics
Afs fractionation trend
PM
OIB
MORB
Ba/Nb
La/Nb
100
10
1
0.5
1
10
(b)
Subduction Metasomatism
Carbonatitic Metasomatism
PM
[Hf/Sm]N
[Ta/La]N
1
0.1
0.1
1

Figure 13

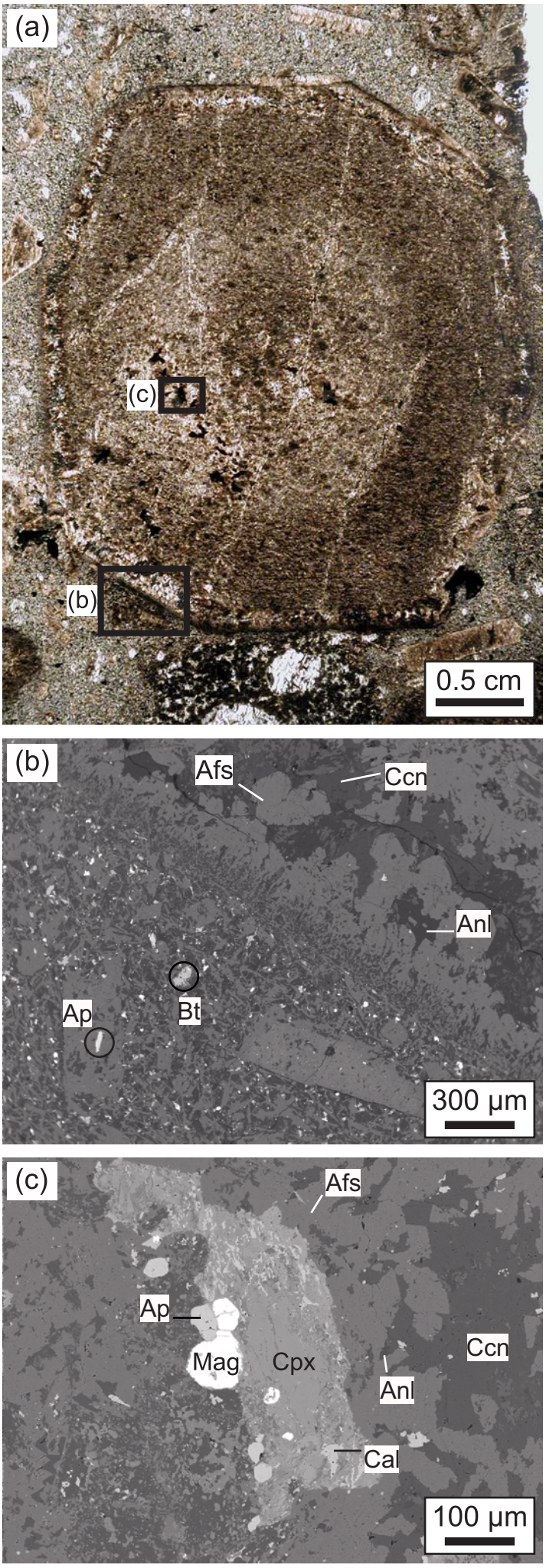
(a)
(c)
(b)
0.5 cm
(b)
Afs
Ccn
Anl
Ap
Bt
300 µm
(c)
Afs
Ap
Mag
Cpx
Ccn
Anl
Cal
100 µm

Table 1: Whole-rock geochemical data for samples from the Tezhsar Alkaline Complex

Lithological Unit	OVU	OVU	OVU	OVU	OVU	OVU	OVU	OVU	OVU	OVU	OVU	OVU	OVU	SYU	SYU	SYU	SYU	SYU	SYU	SYU	SYU	SYU	SYU	SYU	SYU
Sample #	1-2-15	3-1-15	3-2-15	3-3-15	6-1-12	6-2-12	10-43-08	10-44-08	2-8-09	2-11-09	2-12-09	2-13-09	3-2-09	1-4-15	2-1-15	2-8b-15	2-11-15	3-5-15	6-3-12	6-4-12	6-5-12	6-8-12	6-9-12	6-10-12	10-45-08
Field Reference	27	42	43	44	18	19	8	9	2	5	6	7	11	29	30	37	40	46	20	21	22	24	25	26	10
Analysed at	BV	BV	BV	BV	P	P	RHL	RHL	RHL	RHL	RHL	RHL	RHL	BV	BV	BV	BV	BV	P	P	P	P	P	P	RHL
Easting	44.58448	44.57898	44.57822	44.57707	44.53700	44.53700	44.58325	44.58325	44.59320	44.59755	44.59755	44.59862	44.62817	44.58339	44.58454	44.58279	44.59697	44.57256	44.56770	44.56770	44.57538	44.59230	44.57735	44.58232	44.58325
Northing	40.71049	40.72075	40.72034	40.71685	40.66112	40.66112	40.63900	40.63900	40.63365	40.64063	40.64063	40.64185	40.65332	40.70836	40.70469	40.68375	40.69765	40.71180	40.68247	40.68247	40.68107	40.67115	40.69195	40.68042	40.63900
SiO_2	52.92	52.65	51.24	55.57	55.89	56.98	53.90	56.58	56.81	54.78	57.93	59.08	52.13	59.22	60.10	63.15	57.39	56.26	60.86	62.41	59.94	56.89	64.47	59.64	58.66
TiO_2	0.60	0.45	0.59	0.46	0.54	0.50	0.57	0.43	0.54	0.30	0.43	0.48	0.74	0.73	0.46	0.36	0.38	0.35	0.37	0.40	0.36	0.40	0.36	0.57	0.82
Al_2O_3	21.48	20.29	18.24	19.09	20.12	20.66	19.95	20.26	19.91	21.73	19.72	20.61	20.75	19.03	19.35	17.98	19.90	20.72	19.26	18.42	18.56	19.29	17.81	19.24	20.07
Fe_2O_3*	1.64	1.02	1.70	1.22	1.36	0.96	1.66	1.32	1.72	0.63	1.32	1.30	2.60	0.88	0.84	0.77	0.77	0.74	0.86	0.65	0.94	1.05	0.65	0.89	1.07
FeO*	3.45	2.15	3.57	2.57	2.86	2.02	3.49	2.78	3.61	1.33	2.77	2.72	5.45	1.85	1.77	1.62	1.62	1.56	1.81	1.37	1.98	2.20	1.35	1.87	2.25
MnO	0.17	0.22	0.17	0.22	0.14	0.11	0.19	0.20	0.15	0.13	0.11	0.19	0.23	0.22	0.16	0.16	0.15	0.14	0.16	0.12	0.22	0.17	0.07	0.14	0.19
MgO	2.00	0.47	2.80	0.93	0.58	0.44	1.21	0.96	1.83	0.21	0.79	0.77	2.62	0.38	0.35	0.34	0.33	0.45	0.44	0.20	0.59	0.87	0.12	0.40	0.62
CaO	7.76	3.17	5.37	3.57	1.70	2.11	4.43	2.55	4.29	1.72	2.73	2.36	6.71	1.84	1.87	1.24	2.67	2.24	1.80	1.19	2.22	3.13	0.47	2.49	2.02
Na_2O	4.32	4.03	3.93	5.34	5.30	2.01	5.26	4.41	6.07	5.88	5.36	1.90	2.90	4.42	5.66	6.49	5.28	3.59	5.25	4.21	4.86	5.15	6.47	4.76	4.68
K_2O	3.38	10.00	5.46	7.06	7.88	10.73	6.23	8.32	4.65	10.16	6.49	10.52	5.28	8.80	7.83	5.97	7.02	10.67	6.55	8.82	7.10	6.55	6.33	7.39	8.82
P_2O_5	0.45	0.09	0.41	0.31	0.21	0.17	0.30	0.17	0.36	0.05	0.21	0.14	0.54	0.05	0.05	0.09	0.04	0.07	0.09	0.04	0.13	0.20	0.03	0.06	0.06
LOI	0.92	3.88	4.98	2.70	1.73	1.73	4.19	3.11	1.22	2.98	2.78	1.56	0.85	1.63	1.21	0.72	3.23	2.45	1.50	1.28	2.01	3.08	1.12	1.59	0.99
SUM	99.09	98.42	98.46	99.04	98.31	98.42	101.39	101.09	101.17	99.91	100.65	101.62	100.80	99.05	99.65	98.89	98.78	99.24	98.95	99.10	98.91	98.99	99.25	99.04	100.25
Ba	1060	3010	1340	1760	1570	3710	1510	991	1140	460	1110	3940	932	60	144	472	72	272	655	481	1030	891	87	150	208
Co	30.1	17.1	24.9	21	na	na	9.08	6.34	9.23	3.43	6.23	7.35	18.1	13.1	12.7	30.2	77.2	13.1	na	na	na	na	na	na	7.4
Cr	bdl	bdl	bdl	bdl	23	10	2.81	3	2.28	1.65	2.89	3.96	26	bdl	bdl	bdl	bdl	bdl	21	bdl	12	14	12	bdl	3
Cs	2.1	3	0.9	2.9	na	na	6.47	5.63	1.79	3.78	1.34	1.7	5.88	4.8	3.4	4.3	4.7	9.8	na	na	na	na	na	na	2.23
Ga	18	15.7	15.3	16.4	15	17	na	na	na	na	na	na	na	18.7	20.9	21.7	19.5	14.2	19	20	19	20	23	19	na
Hf	2.9	5.1	2.8	4.5	23	10	3.01	11	2.06	3.03	3.24	3.01	2.14	11	11.7	22.4	11	3.4	21	bdl	12	14	12	bdl	6.27
Nb	6.8	18.6	6.6	11.5	12	13	10.5	12.3	8.63	19.2	10.5	11.4	6.95	75.1	61.7	49.5	45.9	16.2	41	59	32	31	45	56	55
Rb	83.2	243	102	191	204	160	157	190	110	321	137	193	186	233	235	261	247	452	251	305	257	197	303	236	175
Sc	bdl	bdl	bdl	bdl	2.9	1.9	3.45	2.19	5.73	0.297	2.75	1.85	13.1	bdl	bdl	bdl	bdl	bdl	1.7	1.3	3.7	4.2	2.9	2.1	1.64
Sn	1	bdl	bdl	bdl	na	na	na	na	na	na	na	na	na	2	2	2	1	bdl	na	na	na	na	na	na	na
Sr	1410	4260	1460	1380	2850	4820	2010	1830	1290	956	1230	3520	1280	885	330	384	2300	959	757	1030	1280	1710	42	1480	817
Ta	0.4	0.9	0.4	0.6	na	na	0.445	3.28	0.543	0.815	0.448	0.474	0.286	3.7	3.1	2.1	2.6	0.9	na	na	na	na	na	na	3.58
Th	8.6	20.9	9	15.7	na	na	10.8	14.7	7.56	18.4	11.6	11.7	7.08	113	124	75.3	77.5	11.6	na	na	na	na	na	na	26.6
U	2.9	6.9	2.7	7	na	na	3.43	5.21	4.07	6.57	4.53	3.64	3.16	9.7	16.7	19.3	15.5	2.6	na	na	na	na	na	na	5.71
V	155	202	212	152	162	145	169	124	160	52.6	112	138	250	84	68	55	63	84	67	55	84	106	35	79	109
Zr	126	271	126	201	263	344	153	189	148	204	166	180	123	494	527	1080	629	168	737	1110	547	549	471	547	304
Y	20.7	39	20.8	33	22	21	28.4	28.7	24.9	26.4	26.3	29.6	23.6	68.7	53	50.3	38	20.8	38	41	29	26	44	31	66
La	36.7	114	42.9	77.8	70	63	72.5	72.9	53.5	80.2	61.2	79.1	45.6	319	244	167	161	81	140	81	71	104	204	75	186
Ce	67.8	199	76.1	138	127	120	125	124	89.9	130	104	135	79.1	558	396	247	264	135	204	224	142	175	328	174	354
Pr	8	22.1	9.1	15.6	14	13	14	13.6	10.2	13.4	11.7	14.8	9.58	59.6	38.5	24.4	26.7	15	23	26	15	17	28	18	39.3
Nd	31.3	78.3	35	58.1	56	54	56.2	53.1	41.1	48.5	46.1	59.5	40	190	117	72.6	84.4	52.4	85	103	61	69	113	70	155
Sm	6	13.5	6.5	10.7	9.3	8.8	10.3	9.7	7.92	8.67	8.49	11.3	8.19	27.2	16.6	10.7	12.5	8.1	13	18	10	10	15	11	28.1
Eu	1.9	3.9	2.1	3.1	2.4	2.8	3.1	2.74	2.33	1.97	2.32	4.47	2.26	3.8	2.2	1.4	1.9	2.3	1.5	2.2	1.9	1.9	0.2	1.6	4.77
Gd	5.2	10.9	5.9	8.8	7.3	7.1	7.58	7.16	5.79	6.48	6.05	7.94	5.82	20.2	12.8	8.2	9.7	6.2	9.5	13	7.7	7.7	11	8	19.7
Tb	0.7	1.4	0.7	1.1	0.94	0.7	1.17	1.19	0.934	1.05	0.988	1.26	0.959	2.6	1.7	1.2	1.3	0.8	1.3	2.1	1.1	1.1	1.8	1.1	2.97
Dy	3.8	7.4	4.1	5.8	5	4.9	4.86	4.93	4.21	4.46	4.34	5.35	4.14	13.7	9.7	7.2	7.4	4	7.5	9.6	5.8	5.6	8.4	6	11.9
Ho	0.7	1.2	0.7	1.1	0.78	0.77	0.895	0.949	0.795	0.821	0.829	0.932	0.773	2.3	1.8	1.4	1.3	0.7	1.5	1.6	1.1	0.94	1.5	1.2	1.98
Er	2.2	3.2	1.9	3	2.2	2.1	2.37	2.43	2.22	2.21	2.35	2.41	2.08	6.1	5.1	4.8	3.7	1.9	3.9	4.2	3	2.6	4.4	3.2	4.88
Tm	0.3	0.5	0.3	0.4	0.36	0.35	0.373	0.457	0.368	0.355	0.389	0.385	0.338	0.8	0.7	0.8	0.6	0.2	0.66	0.68	0.52	0.45	0.75	0.53	0.72
Yb	2.1	2.8	1.9	2.8	2	1.8	2.38	2.56	2.35	2.21	2.52	2.37	2.08	4.3	4.5	6	3.6	1.6	4	3.5	3	2.6	4.6	3.3	4.22
Lu	0.3	0.4	0.3	0.4	0.3	0.27	0.38	0.456	0.4	0.344	0.409	0.38	0.358	0.6	0.6	1	0.5	0.2	0.59	0.45	0.45	0.38	0.57	0.48	0.59
Mo	0.8	0.2	0.5	1.1	na	na	1.11	0.939	1.69	1.08	1.1	2.11	2.21	0.3	1.2	0.6	1.9	0.3	na	na	na	na	na	na	1.01
Cu	165	2.3	117	6.1	na	na	23.8	11.9	24.3	6.77	91.1	29.6	100	7.4	41.3	8.3	45.8	15	na	na	na	na	na	na	7.98
Li	na	na	na	na	na	na	18.4	19.3	22.5	24.9	12.8	21.5	10.8	na	na	na	na	na	na	na	na	na	na	na	29.8
Pb	18.7	12	3.4	25.3	109	55	na	na	na	na	na	na	na	13.1	4.7	18.4	22.4	1.7	97	63	110	83	49	80	na
Zn	83	86	72	97	na	na	89.2	96.2	73.6	72.2	67.9	95.7	120	48	13	65	34	17	na	na	na	na	na	na	92.9
Ni	1.5	0.2	10.6	0.2	na	na	1.4	2.35	0.562	1.52	1.27	3.48	13.6	0.1	0.4	0.5	0.5	0.2	na	na	na	na	na	na	4.56
$^{87}Sr/^{86}Sr$ (measured)					0.704071	0.704002	0.704096	0.704139	0.704111	0.704660	0.704470	0.704057	0.704195								0.704341	0.704205		0.704647	0.704364
$^{87}Sr/^{86}Sr$ (initial)					0.70395	0.70395	0.70397	0.70397	0.70397	0.70410	0.70429	0.70397	0.70395								0.70401	0.70401		0.70438	0.70401
$^{143}Nd/^{144}Nd$ (measured)							0.512859			0.512770		0.512851													0.512849
$^{143}Nd/^{144}Nd$ (initial)							0.512829			0.512741		0.512820													0.512820
ƐNd							4.8			3.0		4.6													4.6
Alkalinity Index (AI)	0.105	0.028	0.058	0.026	0.028	0.056	0.044	0.037	0.046	0.007	0.037	0.056	0.099	0.022	0.015	0.026	0.028	0.032	0.035	0.019	0.028	0.037	0.003	0.033	0.025
FSSI	-0.05	-0.38	-0.12	-0.23	-0.22	-0.02	-0.24	-0.17	-0.15	-0.51	-0.11	0.37	-0.03	-0.1	-0.16	-0.03	-0.38	-0.25	0	0.79	-0.02	-0.12	1.12	-0.05	-0.17

* Fe_2O_3 and FeO contents were calculated based on a Fe^{3+}/Fe_{Total} ratio of 0.3.

Abbreviations: BV = Bureau Veritas, P = Potsdam, RHL = Royal Holloway London, K = Kiel; na = not analysed; bdl = below detection limit

SYU	SYU	SYU	SYU	SYU		CVU	CVU	CVU	CVU	CVU	CVU	CVU
2-7-09	2-9-09	3-3-09	3-5-09	3-6-09		2-3-15	2-4-15	2-6-15	2-7-15	2-8a-15	3-7-09	3-8-09
1	3	12	14	15		32	33	35	36	37	16	17
RHL	RHL	K	RHL	K		BV	BV	BV	BV	BV	RHL	RHL
44.59320	44.59835	44.62075	44.61660	44.61053		44.58697	44.58697	44.58893	44.58929	44.58279	44.60143	44.60703
40.63365	40.63848	40.65353	40.66855	40.67683		40.69464	40.69464	40.69384	40.69375	40.69033	40.67552	40.67572
56.21	51.44	55.14	58.89	60.17		59.14	57.81	55.77	63.47	61.08	60.21	61.49
0.11	0.47	0.36	0.44	0.37		0.37	0.36	0.43	0.32	0.34	0.34	0.36
22.61	20.65	21.91	20.96	19.05		20.13	19.49	21.71	19.61	18.56	20.00	19.63
0.72	1.48	0.65	0.96	0.77		0.99	0.97	0.82	0.53	0.99	1.03	0.95
1.52	3.10	1.37	2.02	1.62		2.07	2.04	1.72	1.11	2.08	2.16	2.00
0.28	0.18	0.22	0.12	0.17		0.18	0.17	0.20	0.05	0.18	0.17	0.16
0.04	0.91	0.16	0.29	0.46		0.70	0.75	0.45	0.27	0.63	0.52	0.42
1.49	4.03	2.13	2.24	2.26		1.85	3.04	3.24	0.17	2.71	2.38	1.92
9.51	4.68	7.63	4.83	5.48		4.95	5.34	7.04	5.91	6.70	6.27	6.25
6.52	9.73	7.94	7.45	6.79		6.97	6.35	3.63	7.57	4.56	6.53	6.79
0.01	0.20	0.03	0.06	0.08		0.15	0.13	0.08	0.04	0.12	0.08	0.07
1.77	2.44	1.15	2.66	1.44		1.84	2.06	4.32	0.88	0.79	1.19	na
100.79	99.31	98.69	100.92	98.66		99.34	98.51	99.41	99.93	98.74	100.88	100.04
9.31	4490	na	170	530		909	906	787	201	1430	546	388
1.55	7.96	na	5.61	na		20.9	43.1	11.3	12.8	4.6	4.81	4.3
2.98	2.55	na	4.24	na		bdl	bdl	bdl	bdl	bdl	8.56	11.7
5.56	2.92	na	6.38	na		5	5.8	1.3	1.1	5	7.36	6.59
na	na	na	na	na		20.2	20.5	19	22.6	19	na	na
10.9	4.2	na	11.1	na		11.2	11.5	4.5	16.4	11.6	13.2	10.5
8.2	18	na	54.4	na		31.5	33.6	19.6	43.2	31	41.8	36.4
407	227	na	226	203		227	205	169	251	183	249	232
0.759	1.04	na	1.04	na		na	na	na	na	na	na	na
na	na	na	na	na		1	1	bdl	2	1	bdl	bdl
50.6	5270	na	573	506		861	1990	984	515	1480	855	403
0.00647	0.752	na	3.12	na		1.4	1.5	0.9	1.8	1	1.71	1.67
31.1	15.4	na	85.5	na		45.4	48.9	24.1	109	60.4	59.6	45.4
10.4	5.73	na	12.7	na		12.1	17.6	3.6	19.9	19.1	19.7	14.6
14.1	230	na	71.9	na		90	89	201	242	82	71.3	66.4
856	273	na	677	na		568	612	284	810	487	723	575
12.3	38.1	na	34.3	na		31.9	31.3	53.9	19	28.4	37.4	37.3
169	96.7	na	191	138		137	114	181	57.3	94.1	133	121
187	171	na	285	220		184	177	246	79	150	204	195
12	18.6	na	25.5	21.4		19.1	17	29.8	11.3	14.5	18.4	18.6
26.3	74.5	na	85	68.1		61.3	55.1	102	36.2	47	62.9	66.6
2.35	14.5	na	13.2	10.8		8.9	8.2	16.1	6.2	7	10.3	11.4
0.338	5.16	na	2.14	2.09		2.1	1.9	4.5	1.1	1.7	2.05	2.22
3.22	10.6	an	10.4	8.85		7	6.5	14	4.1	5.5	8.09	8.73
0.295	1.7	na	1.45	1.18		0.9	0.9	1.7	0.6	0.8	1.25	1.31
1.17	7.04	na	5.91	6.23		5.2	5	9.1	3.5	4.4	5.49	5.81
0.291	1.19	na	1.06	1.17		1	0.9	1.5	0.6	0.8	1.06	1.08
1.1	2.94	na	2.86	3.25		2.8	2.9	4.1	2.2	2.6	3.08	3.02
0.229	0.434	na	0.454	0.488		0.4	0.5	0.6	0.4	0.4	0.561	0.529
1.67	2.64	na	2.73	3.33		3.1	3.2	3.7	2.9	3.1	3.93	3.61
0.365	0.398	na	0.403	0.479		0.5	0.5	0.5	0.5	0.5	0.621	0.582
1.11	1.6	na	1.72	na		0.6	3.7	1.2	2.2	0.3	1.44	2.59
2.33	20.7	na	70.4	na		32	21.1	19	3.2	17.9	29.5	18
66.3	17.7	na	20.9	na		na	na	na	na	na	25	38.5
na	na	na	na	na		20.5	25.2	4.2	20.4	13.7	na	na
181	104	na	77.3	85		60	51	61	55	37	100	88.7
0.796	2.87	na	3.33	16		2.3	0.6	0.5	0.6	0.6	0.881	1.7
0.718557	0.704075	0.706855	0.704695	0.704873							0.704519	0.704987
0.70520	0.70400	0.70424	0.70404	0.70414							0.70404	0.70403
		0.512837										
		0.512813										
		4.4										
-0.003	0.021	0.005	0.047	0.025		0.044	0.038	0.061	0.017	0.026	0.023	0.017
-0.63	-0.55	-0.55	-0.07	-0.07		-0.02	-0.11	-0.16	-0.01	-0.03	-0.16	-0.13

Table 2: Argon isotopic data for an amphibole separate of syenite sample 6-8-12.

TZ-6-8-12 Laboratory ID: C15038 Irradiation ID: PO-2

J=0.0009720	$^{40}Ar/^{39}Ar$			$^{37}Ar/^{39}Ar$			$^{36}Ar/^{39}Ar$ ($\times10^{-3}$)			K/Ca	$^{40}Ar^*$ (%)	$^{39}Ar_K$ fraction (%)	$^{40}Ar^*/^{39}Ar_K$			Age (Ma)	±	1s
Laser output																		
1.8%	1397	±	251	7.4	±	137	3703	±	710.85	0.08	21.73	0.13	305	±	98	469	±	132
2.0%	1385	±	938	141	±	566	4558	±	3110	0.00	3.54	0.03	54	±	147	93	±	245
2.4%	352	±	60	6	±	149	919	±	203	0.10	22.92	0.14	81	±	44	137	±	71
2.8%	77	±	3	39	±	15	141	±	33	0.01	49.59	0.82	39	±	10	67	±	17
3.1%	37.0	±	0.4	7	±	4	42	±	5	0.09	67.55	4.85	25.1	±	1.4	44	±	2
3.3%	29.79	±	0.16	6	±	2	20	±	3	0.10	81.79	13.29	24.5	±	0.9	42.4	±	1.5
3.5%	29.80	±	0.14	1.6	±	1.7	18.7	±	1.7	0.37	81.82	21.93	24.4	±	0.5	42.3	±	0.9
3.7%	30.8	±	0.2	2.4	±	0.6	26.9	±	1.0	0.25	74.79	46.26	23.1	±	0.4	40.0	±	0.6
3.9%	31.1	±	0.4	2.4	±	1.9	27	±	3	0.25	74.67	12.56	23.3	±	0.9	40.4	±	1.5

Total gas age	42.05	±	0.52
Plateau age (step 5-9: 98.8% of total ^{39}Ar)	**40.96**	**±**	**0.46**
Normal isochron age (step 5 to 9)	41.32	±	2.51
Inverse isochron age (step 5 to 9)	41.25	±	2.11

Supplementary material

Whole rock major and trace element analyses

1. Royal Holloway University, London, UK

Fourteen samples were analysed by inductively coupled plasma atomic emission spectrometry (ICP-AES) for major elements and some high abundance trace elements (Sr, Zr, Cr, Sc, Zn, Co, Li, V, Be and Ni) and by inductively coupled plasma mass spectrometry (ICP-MS) for low abundance trace elements (Rb, Nb, Y, Mo, Cs, Ba, Hf, Ta, Tl, Pb, Th, U, and all REE) using a Perkin Elmer instrument. The analytical work followed the methodology described by Walsh et al. (1981) and Garbe-Schönberg (1993), respectively. The relative standard deviation (RSD) typically was ≤ 2% for major elements and ≤ 5% for minor and trace elements.

2. Institute of Geosciences, Kiel University, Germany

Three samples were analysed by X-ray fluorescence (XRF) on fused glass discs using a Philips PW1480 XRF spectrometer for major elements and by ICP-MS using an Agilent 7500c instrument for trace elements. For major element oxides, the RSD is ≤1.3 % based on multiple analyses of reference material BHVO-1. The RSD for trace elements is generally ≤2 % based on multiple analyses of one sample solution. Details about sample preparation and instrument calibration are given in Garbe-Schönberg (1993) and John et al. (2008), and representative data for precision and accuracy during the course of this study are provided by Laeger et al. (2013).

3. GeoForschungsZentrum (GFZ) Potsdam and Potsdam University, Germany

Nine samples were analysed for major and some trace elements (Ba, Cr, Ga, Nb, Ni, Rb, Sr, V, Y, Zn and Zr) by XRF using a Siemens SRS303-AS XRF spectrometer at the GFZ and for REE by ICP-AES using a Varian Vista MPX instrument following the methods described by Zuleger and Erzinger (1998). RSD values are in the range of 1-3% for major oxides and ≤ 5% for trace elements and REE (Moazzen and Oberhänsli, 2008; Hadj Zobir et al., 2014).

4. AcmeLabs, Bureau Veritas Minerals, Vancouver, Canada

Fifteen samples were analysed for major elements by XRF using a Panalytical Axios Max instrument and by ELAN 9000 ICP-MS for trace elements and REE. The RSD is <1.2% for major oxides based on the analyses of SY-4(D) diorite gneiss and OREAS72B VMS ore standards, while for trace elements and REEs the RSD was <3.8%.

Strontium (Sr) and neodymium (Nd) isotope analyses

Strontium (Sr) and neodymium (Nd) isotope analyses were performed on a Thermo Finnigan Triton multicollector mass spectrometer at the School of Earth and Environment, University of Leeds. About 30 to 60 mg of powdered whole-rock material (same was used for the major and trace element work) was dissolved in concentrated ultra-clean HF-HNO_3-HCl acids and Sr and Nd were extracted from the unspiked solutions by conventional ion-exchange chromatographic techniques (see Halama et al. 2013 for details of the analytical protocol). $^{87}Sr/^{86}Sr$ and $^{143}Nd/^{144}Nd$ ratios were normalized for mass fractionation to $^{86}Sr/^{88}Sr = 0.1194$ and $^{146}Nd/^{144}Nd = 0.7219$. The average $^{87}Sr/^{86}Sr$ obtained from replicate measurements of NIST SRM-987 during this study was 0.710254 and all data were corrected for the offset from the generally accepted value 0.710250 (McArthur et al. 2000). Similarly, Nd isotope data were corrected for the offset from the LaJolla reference material ($^{143}Nd/^{144}Nd = 0.511853$; Weis et al. 2005). Initial $^{87}Sr/^{86}Sr$ isotope ratios were calculated using the ^{87}Rb decay constant 1.3972×10^{-11} a^{-1} (Villa et al. 2015). For the calculations of the εNd values, the following parameters were used: ^{147}Sm decay constant $\lambda = 6.54 \times 10^{-12}$ a^{-1}, present-day $(^{143}Nd/^{144}Nd)^{CHUR} = 0.512638$, $(^{147}Sm/^{144}Nd)^{CHUR} = 0.1966$.

$^{40}Ar/^{39}Ar$ dating

About 1 mg of amphibole from syenite sample 6-8-12 was used for $^{40}Ar/^{39}Ar$ analysis by the CO_2 laser stepwise heating technique at the Institute of Earth and Environmental Science,

Universität Potsdam. For details of the analytical protocol see Wilke et al. (2010) and Halama et al. (2014). Mineral grains were obtained by crushing, sieving and selecting the size fraction between 250-500 μm mesh size for magnetic separation and finally by hand-picking under the binocular. Separated amphiboles were cleaned ultrasonically in 10% HNO_3 for 15 minutes and then washed in de-ionized water and dried. Samples, the Fish Canyon Tuff sanidine age standard, prepared by the Geological Survey of Japan (27.5 Ma: Uto et al., 1997; Ishizuka, 1998) and salts of K_2SO_4 and CaF_2 were irradiated at the Oregon State TRIGA Reactor for 4 hours under a neutron flux of $2.5x10^{13}$ n cm^{-2} s^{-1}. Argon isotope ratios of the gas from the samples were analyzed by stepwise heating until total fusion using a New Wave Research DualWave laser ablation system comprising a 50W CO_2 continuous laser with 10.6 μm wavelength. The extracted gas is purified in the ultra-high vacuum line via SAES getter pumps and a cold trap for 10 min. The high sensitivity Micromass 5400 noble gas mass spectrometer used for Ar isotopic analysis is equipped with an electron multiplier pulse counting system for analyzing small amounts of Ar. Raw data were corrected for procedural blank contributions, mass discrimination by analysis of atmospheric Ar, interferences of Ar isotopes derived from Ca and K and decay of radiogenic ^{37}Ar and ^{39}Ar isotopes produced by irradiation. Calculation of ages and errors was performed following Uto et al. (1997) using the total ^{40}K decay constant of 5.543×10^{-10} a^{-1} (Steiger and Jäger, 1977) as well as decay constants of 1.978×10^{-2} d^{-1} for ^{37}Ar and 2.58×10^{-3} a^{-1} for ^{39}Ar.

References:

Garbe-Schönberg, C.-D., 1993. Simultaneous determination of thirty-seven trace elements in twenty-eight international rock standards by ICP-MS. Geostandards Newsletter 17:81–97.

Hadj Zobir, S., Altenberger, U., Günter, C., 2014. Geochemistry and petrology of metamorphosed submarine basic ashes in the Edough Massif (Cap de Garde, Annaba, northeastern Algeria). Comptes rendus - Geoscience 346:244-254.

Halama, R., Konrad-Schmolke, M., Sudo, M., Marschall, H.R., Wiedenbeck, M., 2014. Effects of fluid–rock interaction on $^{40}Ar/^{39}Ar$ geochronology in high-pressure rocks (Sesia-Lanzo Zone, Western Alps). Geochimica et Cosmochimica Acta 126:475–494.

Halama, R., Savov, I.P, Garbe-Schönberg, D., Schenk, V., Toulkeridis, T., 2013. Vesuvianite in high-pressure-metamorphosed oceanic lithosphere (Raspas Complex, Ecuador) and its role for transport of water and trace elements in subduction zones. European Journal of Mineralogy 25:193–219.

Ishizuka, O., 1998. Vertical and horizontal variations of the fast neutron flux in a single irradiation capsule and their significance in the laser-heating $^{40}Ar/^{39}Ar$ analysis: Case study for the hydraulic rabbit facility of the JMTR reactor, Japan. Geochemical Journal 32: 243-252.

John, T., Klemd, R., Gao, J., Garbe-Schönberg, C.-D., 2008. Trace-element mobilization in slabs due to non-steady-state fluid-rock interaction: Constraints from an eclogite-facies transport vein in blueschist (Tianshan, China). Lithos 103:1–24.

Laeger, K., Halama, R., Hansteen, T., Savov, I.P., Murcia, H.F., Cortés, G.P., Garbe-Schönberg, D., 2013. Crystallization conditions and petrogenesis of the lava dome from the ~900 years BP eruption of Cerro Machín Volcano, Colombia. Journal of South American Earth Sciences 48:193-208.

McArthur, J.M., Donovan, D.T., Thirlwall, M.F., Fouke, B.W., Mattey, D., 2000. Strontium isotope profile of the early Toarcian (Jurassic) oceanic anoxic event, the duration of ammonite biozones, and belemnite palaeotemperatures. Earth and Planetary Science Letters 179:269–285.

Moazzen, M., Oberhänsli, R., 2008. Whole rock and relict igneous clinopyroxene geochemistry of ophiolite-related amphibolites from NW Iran – Implications for protolith nature. Neues Jahrbuch für Mineralogie – Abhandlungen 185:51-62.

Steiger, R.H., Jäger, E., 1977. Subcommission on geochronology: Convention on the use of

decay constants in geo- and cosmochronology. Earth and Planetary Science Letters 36: 359-362.

Uto, K., Ishizuka O., Matsumoto A., Kamioka H., Togashi S., 1997. Laser-heating $^{40}Ar/^{39}Ar$ dating system of the Geological Survey of Japan: system outline and preliminary results. Bulletin of Geological Survey of Japan 48:23–46.

Villa, I.M., DeBievre, P., Holden, N., Renne, P.R., 2015. IUPAC-IUGS recommendation on the half life of ^{87}Rb. Geochimica et Cosmochimica Acta 164:382-385.

Walsh, J. N., Buckley, F., J. Barker, 1981. The simultaneous determination of the rare-earth elements in rocks using inductively coupled plasma source spectrometry. Chemical Geology 33:141–153.

Weis, D., Kieffer, B., Maerschalk, C., Pretorius, W., Barling, J., 2005. High-precision Pb-Sr-Nd-Hf isotopic characterization of USGS BHVO-1 and BHVO-2 reference materials. Geochemistry, Geophysics, Geosystems, 6, Q02002, doi:10.1029/2004GC000852.

Wilke F. D. H., O'Brien P. J., Gerdes A., Timmerman M. J., Sudo, M., Khan M. A., 2010. The multistage exhumation history of the Kaghan Valley UHP series, NW Himalaya, Pakistan from U–Pb and 40Ar/39Ar ages. European Journal of Mineralogy 22:703–719.

Zuleger, E., Erzinger, J., 1988. Determination of the REE and Y in silicate materials with ICP-AES. Fresenius Journal of Analytical Chemistry 332:140-143.